China Geology 9 (2026) 635−651

China Geology

Journal homepage: http://chinageology.cgs.cn
https://www.sciencedirect.com/journal/china-geology

Geological structure controls CO_2 hydrate sequestration in seafloor sediments: A numerical simulation study of anticline, syncline, and inclined reservoirs

Shu-xia Li[a, b, c,*], Zhong-xue Song[a, b, c], Yang Guo[a, b, c], Gao-wei Hu[d, e], Lu Liu[a, b, c], Hao Sun[a, b, c], Ben-kui Lou[a, b, c], Jun-hao Liu[a, b, c], Zhen-hao Ren[a, b, c]

[a] *School of Petroleum Engineering*, *China University of Petroleum* (*East China*), *Qingdao* 266580, *China*
[b] *State Key Laboratory of Deep Oil and Gas*, *China University of Petroleum* (*East China*), *Qingdao* 266580, *China*
[c] *Shandong Key Laboratory of Offshore Oil & Gas and Hydrates Development*, *China University of Petroleum* (*East China*), *Qingdao* 266580, *China*
[d] *The Key Laboratory of Gas Hydrate*, *Ministry of Natural Resources*, *Qingdao Institute of Marine Geology*, *China Geological Survey*, *Qingdao* 266237, *China*
[e] *Laboratory for Marine Mineral Resources*, *Qingdao Marine Science and Technology Center*, *Qingdao* 266237, *China*

ARTICLE INFO

Article history:
Received 21 July 2025
Received in revised form 1 November 2025
Accepted 9 December 2025
Available online 4 June 2026

Keywords:
CO_2 hydrate sequestration
Geological structures
Horizontal+inclined+anticline+syncline
Numerical simulation
Structural dip angle
Phase Equilibrium zone
Sequestration capacity
Sequestration safety
Carbon neutrality
CCS

ABSTRACT

Sequestration of CO_2 as hydrates in seafloor sediments is an effective method for reducing CO_2 emissions. However, the efficiency of CO_2 hydrate sequestration can be influenced by the geological structure of seafloor reservoirs. To address this, the authors numerically investigate the effects of four reservoir structures (horizontal, inclined, anticline, and syncline) and dip angle on CO_2 hydrate formation mass and sequestration security. The results show that different geological structures alter the temperature distribution within the reservoir, thereby modifying the stability zone of CO_2 hydrates. At a dip angle of 30°, the hydrate formation mass (F_{hyd}) in the inclined, anticline, and syncline structures changes by −19.12%, +6.60%, and −7.19%, respectively, relative to the horizontal structure (baseline: 342×10^6 kg). The distance from the top of the CO_2 hydrate cap to the seafloor mudline (D_H), a key security indicator, varies significantly: Compared to 25 m in the horizontal structure, D_H changes by +160%, −20%, and +20% for the inclined, anticline, and syncline structures, respectively. As the dip angle increases, F_{hyd} in the anticline structure increases while D_H decreases. In contrast, F_{hyd} decreases and D_H increases in both the inclined and syncline structures. The temperature variation across structures is a key factor influencing F_{hyd}, while permeability is a major factor affecting the safety of CO_2 sequestration. Therefore, if F_{hyd} is the sequestration objective, the anticline structure is the optimal reservoir. If D_H is the objective, the inclined structure is the best reservoir. These findings provide critical insights for site selection in marine CO_2 hydrate sequestration projects.

©2026 China Geology Editorial Office.

1. Introduction

With the continuous increase in global carbon emissions and the intensification of the greenhouse effect, global temperatures are exhibiting an upward trend (Samset BH et al., 2024; Scafetta N, 2024). This has given rise to a series of environmental challenges, including the frequent occurrence of extreme weather events, rising sea levels, and a decline in biodiversity (Saxena P et al., 2024; Sani M et al., 2025; Zhao Y and He Q, 2025). In this context, CO_2 sequestration technology has garnered widespread attention as an effective method for emission reduction. Large-scale CO_2 sequestration methods primarily include geological sequestration and marine sequestration (Aminu MD et al., 2017; Zhao YF and Itakura KI, 2023). Current research predominantly focuses on geological sequestration, which includes three main types: Sequestration in depleted oil and gas reservoirs (Li ZW et al., 2006; Akai T et al., 2021; Wei B et al., 2023), in saline aquifers (Yang F et al., 2010; Luo A et al., 2022; Izadpanahi A et al., 2024), and in coal seams lacking mining value (Shi JQ and Durucan S, 2005; Liu SQ et al., 2023; Wu M et al., 2023). However, large-scale CO_2 injection into onshore reservoirs may induce geomechanical problems (Stork AL et al., 2018; Kuang NJ et al., 2023), potentially increasing the

First author: *E-mail address*: lishuxia@upc.edu.cn (Shu-xia Li).

* Corresponding author: *E-mail address*: lishuxia@upc.edu.cn (Shu-xia Li).

Literary editor: Xi-jie Chen
doi:10.31035/cg2025193
2096-5192/© 2026 China Geology Editorial Office.

Copyright © 2026 Editorial Office of China Geology. Publishing services by Elsevier B.V. on behalf of KeAi Communications Co. Ltd.
This is an open access article under the CC BY-NC-ND License (http://creativecommons.org/licenses/by-nc-nd/4.0/).

risk of CO_2 leakage. Marine sequestration typically involves CO_2 sequestration either in the form of liquid lakes or as CO_2 hydrates in seafloor reservoirs (Ling ZY et al., 2024). The sequestration of CO_2 in the form of liquid lakes may lead to ocean acidification, potentially affecting marine ecosystems (McMinn A et al., 2014; Dehghani MR et al., 2024). However, CO_2 hydrate sequestration in seafloor sediments is considered one of the most promising methods for carbon reduction (Jia SJ et al., 2024). The formation of CO_2 hydrates can mitigate ocean acidification (Zheng JJ et al., 2020), and the vast storage capacity of seafloor reservoirs enables substantial CO_2 sequestration (Adams EE and Caldeira K, 2008). Additionally, CO_2 hydrates exhibit high stability, while their formation reduces reservoir permeability, thereby enhancing sequestration security (Cao XW et al., 2022; Zhao GJ et al., 2023). Thus, seafloor CO_2 hydrate sequestration offers multiple advantages that improve safety, making it a highly promising method for future development.

Previous studies employing both experimental and numerical simulation methods have demonstrated the feasibility of CO_2 sequestration using hydrates (Tohidi B et al., 2010; Qanbari F et al., 2012; Almenningen S et al., 2019). The formation of CO_2 hydrates reduces pore volume, while pore water in narrow pore spaces exhibits significant capillary forces that effectively prevent CO_2 leakage (Zhao GJ et al., 2022). The sequestration of CO_2 hydrates exhibits a self-capturing effect (Kim HS and Cho GC, 2019), where the formed hydrate cap can inhibit upward CO_2 migration, providing a safeguard for CO_2 storage within seafloor sediments (Yamaguchi AJ et al., 2023). Furthermore, when the seafloor reaches a critical depth, a negative buoyancy zone for CO_2 develops in sedimentary reservoirs as CO_2 density exceeds that of seawater. This phenomenon provides an additional safety mechanism for hydrate-based CO_2 sequestration (House KZ et al., 2006; Qanbari F et al., 2011; Kumar Y and Sangwai JS, 2023). Experimental studies on the kinetics of CO_2 hydrate formation from both gaseous and liquid CO_2 have revealed that liquid CO_2 hydrates form at faster rates (Li N et al., 2022; Zhang XM et al., 2022), exhibiting higher sequestration capacity (Chen HN et al., 2024).

The sequestration of CO_2 hydrates in porous media is influenced by multiple factors. To enhance both the storage capacity and security of CO_2 hydrate sequestration in seafloor sediments, researchers have investigated key geological factors affecting CO_2 hydrate formation. The formation of a low-permeability hydrate cap depends primarily on the absolute permeability of the target sedimentary formation (Sawano Y et al., 2022). Permeability heterogeneity enhances CO_2 capture through combined gravitational and capillary forces (Dai ZX et al., 2017). Moreover, greater permeability anisotropy promotes CO_2 hydrate storage efficiency (Xia YQ et al., 2024). Through experimental investigations, Zhou XB et al. (2025) demonstrated that reduced initial water saturation in sedimentary reservoirs negatively impacts CO_2 hydrate phase equilibrium. Gu YH et al. (2025) utilized self-developed thermo-hydro-chemical (T-H-C) coupled numerical model to analyze the influence of geological parameters on CO_2 hydrate stability and sequestration efficiency. Their results demonstrate that reservoir thermal conductivity exerts a more pronounced effect than permeability. Regarding geological factors, previous studies have primarily focused on the effects of sediment permeability (Lou BK et al., 2025), water saturation (Ning YX et al., 2025), and thermal properties (Wei RP et al., 2021) on the efficiency and safety of CO_2 hydrate sequestration. However, most of these studies were based on an idealized horizontal reservoir and did not adequately considered variations in fluid migration pathways and hydrate formation characteristics under different geological structures. The coupling between structure-controlled fluid migration and hydrate formation remains insufficiently investigated.

In addition to geological factors, operational factors affecting CO_2 hydrate sequestration have also been investigated. Using magnetic resonance imaging (MRI) technology, Sun HR et al. (2024) examined how injection rate and reservoir pressure influence hydrate formation dynamics. The results indicate that higher injection rates and initial reservoir pressures promote hydrate formation; however, under conditions of high reservoir pressure and low injection rate, hydrate formation may result in wellbore blockage. Teng YH and Zhang DX (2018) conducted numerical simulations using TOUGH+HYDRATE software to evaluate CO_2 hydrate sequestration under various geological conditions, demonstrating its safety and long-term stability in marine sediments. Zhang K et al. (2022) established that controlled reservoir pressure effectively mitigates wellbore blockage during CO_2 injection in hydrate stability zones, thereby improving sequestration capacity. Through CMG-STARS simulations, Liu Z et al. (2023) confirmed that hydraulic fracturing significantly reduces wellbore blockage induced by CO_2 hydrates in depleted CH_4 reservoirs. Guo Y et al. (2024) revealed a non-monotonic relationship between sequestration capacity and fracture length, characterized by an initial increase followed by decrease. Cui JL et al. (2021) determined that lower injection temperatures and rates facilitate formation of more stable CO_2 hydrate caps. Employing COMSOL simulations, Xia YQ et al. (2025) demonstrated that: (1) Higher single-well injection rates accelerate hydrate cap formation while reducing the dissolved CO_2 sequestration efficiency; and (2) reduced well spacing in dual horizontal well configurations promote larger hydrate cap formation. Regarding injection parameters, although many studies have examined the influence of injection rate, pressure, temperature, and well location on CO_2 hydrate formation, the effect of geological structure on these parameters has generally been neglected. Structural differences can alter reservoir temperature and pressure conditions, thereby further changing the influence of injection parameters on hydrate formation.

Most prior studies assume horizontal reservoirs, yet real seafloor structures are inclined or folded. How structure and

dip angle couple to control hydrate formation remains unclear. Seismic profiles of submarine reservoirs from four different regions: (1) Shenhu area, China (Su M et al., 2016); (2) Krishna-Godavari Basin (Collett TS et al., 2019); (3) Northern Gulf of Mexico (Boswell R et al., 2009); (4) Ulleung Basin, Korea (Ryu BJ et al., 2013). These data demonstrate the necessity of considering reservoir structure when evaluating CO_2 hydrate formation dynamics in subsea sediments.

To address this knowledge gap, this study establishes four representative structural models (horizontal, inclined, anticline, and syncline) through numerical simulations, systematically investigating how geological structure governs CO_2 hydrate formation and spatial evolution.

2. Mathematical model

This study employs the reservoir simulation software CMG-STARS to simulate the processes of CO_2 hydrate formation and dissociation. According to the CO_2 phase equilibrium curve, CO_2 is in a liquid state under the temperature and pressure conditions simulated in this study. To better distinguish between CO_2 and water components, CO_2 is treated as the oil phase in the simulation. The mathematical model includes three phases, namely oil, water, and CO_2 hydrate, and three components, namely water, CO_2, and hydrate. It is assumed that the flow of the oil and water phases in the porous medium of the reservoir follows Darcy's law. CO_2 hydrate is considered an immobile solid phase, and its formation leads to changes in the reservoir porosity and permeability.

2.1. Mass balance equations

Based on the above assumptions and the principle of mass conservation, considering the effects of fluid flow, chemical reactions, and source-sink terms, the mass conservation equations for each component are as follows (Eqs. 1–3):

$$\partial(\varphi\rho_c S_c)/\partial t = \nabla\cdot(\rho_c v_c) + q_c + m_c \tag{1}$$

$$\partial(\varphi\rho_w S_w)/\partial t = \nabla\cdot(\rho_w v_w) + m_w \tag{2}$$

$$(\varphi\rho_h S_h)/\partial t = m_h \tag{3}$$

where the subscripts c, w and h represent CO_2, water, and CO_2 hydrate, respectively. φ is the porosity of the reservoir (a decimal); ρ is the density (kg/m^3); v is the flow rate (m/s); S is the saturation (a decimal); q is the source-sink term [kg/(m^3·s)]; and m is the mass of CO_2 hydrate formed or dissociated per unit volume per unit time [kg/(m^3·s)].

2.2. Energy conservation equations

Considering the effects of heat conduction, heat convection, hydrate formation and dissociation reactions, and source-sink terms in the reservoir, the energy conservation equation per unit volume is as follows (Eqs. 4–6):

$$\partial(C_{\text{eff}}T)/\partial t = \nabla\cdot(\lambda_{\text{eff}}\nabla T) + \nabla\cdot\left[\left(\sum_{\alpha=c,w}\rho_\alpha v_\alpha C_\alpha\right)T\right] + q_c C_c T + n_h \Delta H_h \tag{4}$$

$$C_{\text{eff}} = (1-\varphi)\rho_R C_R + \sum_{\alpha=c,w,h}\varphi S_\alpha \rho_\alpha C_\alpha \tag{5}$$

$$\lambda_{\text{eff}} = (1-\varphi)\lambda_R + \sum_{\alpha=c,w,h}\varphi S_\alpha \lambda_\alpha \tag{6}$$

where the subscripts R represent the sediment; T represents the temperature (K); C represents the specific heat capacity [J/(kg·K)]; λ represents the thermal conductivity [W/(m·K)]; n_h refers to the amount of substance for hydrate formation or dissociation per unit volume per unit time [mol/(m^3·s)]; and ΔH_h is the heat released or absorbed per mole of hydrate formed or dissociated (J/mol).

2.3. Kinetic model for hydrate formation and dissociation

The chemical equation for the formation and dissociation of CO_2 hydrate is as follows (Eq. 7):

$$CO_2 + nH_2O \leftrightarrow CO_2\cdot nH_2O \pm \text{heat} \tag{7}$$

where n is the hydrate number of the hydrate molecule, with a value of 5.75 (Wang PF et al., 2024).

The rate of CO_2 hydrate formation and dissociation is described by the Kim-Bishnoi model as follows (Kim HC et al., 1987) (Eqs. 8–9):

$$dc_h/dt = (k_h A_{HS}/\rho_w\rho_h)(\phi S_w\rho_w)(\phi S_h\rho_h) p_e(1-1/K(p,T))\exp(-\Delta E/RT) \tag{8}$$

$$k_h = \begin{cases} k_f \\ k_d \end{cases} \tag{9}$$

where k_f is the intrinsic formation rate of the hydrate [mol/(m^2·kPa·d)]; k_d is the intrinsic dissociation rate of the hydrate [mol/(m^2·kPa·d)]; c_h is the hydrate concentration (mol/m^3); A_{HS} is the specific surface area of the hydrate solid (m^2/m^3); ΔE is the activation energy (J/mol); R is the gas constant [8.314 J/(mol·K)]; p_e is the equilibrium pressure (kPa); and K is the equilibrium constant.

2.4. Porosity and permeability dynamic model

In the simulation, hydrates form and exist as a solids phase, occupying the pore space. This study employs the Carmen-Kozeny equation (Carman PC, 1997) to determine how porosity varies with hydrate saturation, from which permeability is subsequently calculated (Eqs. 10–11).

$$\varphi = \varphi_0(1-S_h) \tag{10}$$

$$k = k_0(\varphi/\varphi_0)^{ck}((1-\varphi_0)/(1-\varphi))^2 \tag{11}$$

where φ_0 and φ represent the initial porosity and effective porosity of the reservoir (a decimal), k_0 and k represent the initial permeability and effective permeability of the reservoir (mD), and ck is an empirical coefficient representing the permeability reduction exponent, with a value of 5.

2.5. Initial conditions

The model assumes atmospheric pressure at sea level and a constant temperature T_0 at the seafloor mudline. Initial reservoir pressure and temperature distributions are calculated using hydrostatic and geothermal gradients, given by Eqs. 12–13.

$$P = P_0 + \Delta P \times (H + H_1) \tag{12}$$

where P is the pressure at the calculation point (kPa); P_0 is the atmospheric pressure (kPa); ΔP is the hydrostatic pressure gradient (9.8 kPa/m); H is the depth from sea level to the seafloor (m); and H_1 is the depth from the seafloor to the calculation point (m).

$$T = T_0 + \Delta T \times H_1 \tag{13}$$

where T is the temperature at the calculation point (°C); T_0 is the temperature at the seafloor (°C); ΔT is the geothermal gradient (°C/m).

3. Simulation model

3.1. Benchmark model of horizontal structure

Geological data from the SH7 site in the Shenhu area were utilized for numerical simulations of CO_2 hydrate sequestration. The SH7 site is favorable for CO_2 hydrate formation, with a water depth of 1108 m, a seafloor temperature of 4.5°C and a pressure of 11.7 MPa. Fig. 1 illustrates the thickness map of the CO_2 hydrate stability zone at the SH7 site. The black curve represents the phase equilibrium curve of CO_2 hydrate, the blue dashed line indicates the gas-liquid phase equilibrium curve of CO_2, the orange solid line marks the seafloor mudline, and the red solid line indicates the geothermal gradient of the reservoir. The green region denotes the CO_2 hydrate stability zone. The thickness of the CO_2 hydrate stability zone (HSZ) is defined as the vertical distance between the seafloor and the intersection point of the CO_2 hydrate phase equilibrium curve with the geothermal gradient curve (Imaoka T et al., 2024). At the SH7 site, the HSZ extends from 1108 m to 1251 m below seafloor, yielding a calculated thickness of 143 m. The CO_2 gas-liquid equilibrium curve indicates that injected CO_2 remains liquid under reservoir conditions.

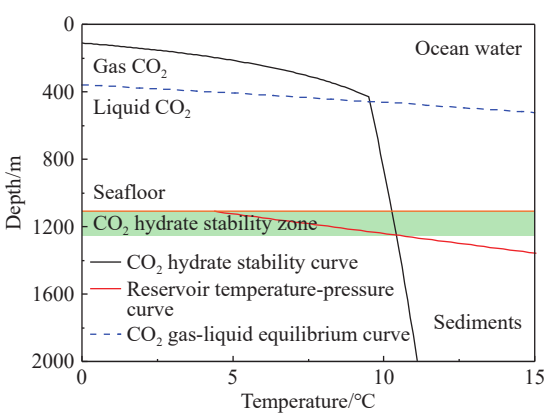

Fig. 1. Thickness map of the CO_2 hydrate stability zone at the SH7 site.

Using geological data from the SH7 site (Li SX et al., 2021), this study established a horizontal benchmark model for CO_2 hydrate sequestration simulation, as shown in Fig. 2. The model domain measures 1010 m × 1010 m × 300 m, discretized into 101×101×60 grid blocks. A 300 m thick sedimentary reservoir was defined below the seafloor, with horizontal and vertical permeabilities of 75 mD and 15 mD, respectively (Dai S et al., 2019). Constant-pressure conditions were applied at the upper and lower boundaries. Key model parameters are summarized in Table 1, and CO_2 hydrate properties are provided in Table 2.

To ensure effective CO_2 injection and long-term sequestration while avoiding premature hydrate formation near the wellbore, the injection point was positioned below the CO_2 hydrate stability zone. A vertical well with a 10 m perforation interval was placed 170 m below the seafloor. The injected liquid CO_2 temperature was maintained at 11.7°C to match reservoir conditions, enabling high injection rates. To

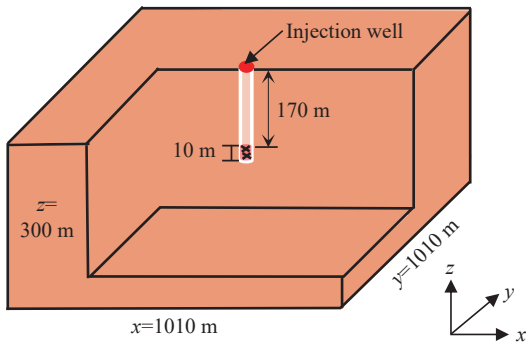

Fig. 2. Benchmark model for CO_2 hydrate sequestration in horizontal reservoirs.

Table 1. Main parameters for numerical simulations.

Parameter	Value
Reservoir porosity (φ)	0.4
Reservoir horizontal permeability/mD	75
Reservoir vertical permeability/mD	15
Pressure at the seafloor mudline/MPa	11.7
Temperature at the seafloor mudline/°C	4.5
Geothermal gradient/(°C/km)	43
Water saturation (S_w)	1.0
Rock thermal conductivity/[W/(m·K)]	1.35
Water thermal conductivity/[W/(m·K)]	0.6
CO_2 thermal conductivity/[W/(m·K)] (Guo Y et al., 2024)	0.105
Rock heat capacity/[J/(kg·K)]	742
Water heat capacity/[J/(kg·K)]	4200
CO_2 heat capacity/[J/(kg·K)] (Guo Y et al., 2024)	1436

prevent reservoir fracturing from excessive pressure, the injection pressure was set to 17.48 MPa (1.3 times the reservoir pressure) (Jing J et al., 2023). The liquid CO_2 injection rate was maintained at 300 t/d for 10 continuous years, achieving a cumulative injection of approximately 1×10^6 t. The simulation period spanned 500 years of CO_2 sequestration.

3.2. Establishment of the geological structure model

Fig. 3 illustrates the different structural types of seafloor reservoirs. The angle between the inclined direction and the horizontal direction defines the dip angle of the inclined structure. The interlimb angle represents the angles of different anticline and syncline structures (Li YB et al., 2024). The dip angles of the wings of the anticline and syncline are correlated with the dip angle of the inclined structure, forming a unified dip angle.

3.2.1. Establishment of the inclined structure model

Fig. 4 illustrates the distribution of the top reservoir layer in inclined structures with varying dip angles. According to previous studies, the dip angles of hydrate-bearing reservoirs typically range from 0° to 40° (Li YB et al., 2024). In this study, four cases were designed with reservoir dip angles of 0°, 10°, 20°, and 30°. To ensure consistent temperature and pressure conditions at the vertical well injection point across different structural models, the inclined structure model is constructed based on the center position of the horizontal model. This approach minimizes the influence of extraneous factors on hydrate formation.

Fig. 5 shows the distributions of initial pressure, temperature and CO_2 hydrate stability zone in inclined structures with varying dip angles. The pressure contours of the different inclined structures are horizontal and unaffected by the dip angle. The pressure distribution increases with depth. In contrast, the temperature contours are notably affected by the reservoir dip angle. As the dip angle increases, the temperature contours shift accordingly. At the same depth, reservoirs with larger dip angles exhibit greater temperature differences between the upper and lower sections. Since the CO_2 hydrate stability zone is controlled by both temperature and pressure distributions, it forms an angle with the horizontal direction. This angle increases with the reservoir dip.

Table 2. Main Parameters of CO_2 hydrate.

Parameter	Value
CO_2 density at injection location ρ/(kg/m^3)	934.5
Molar mass of hydrate M_m /(g/mol) (Uddin M et al., 2008)	147.5
CO_2 hydrate density ρ/(kg/m^3) (Uddin M et al., 2008)	1100
Hydrate dissociation rate constant k_d/[mol/(m^2·kPa·d)] (Uddin M et al., 2008)	10.71×10^{12}
Hydrate formation rate constant k_f/[mol/(m^2·kPa·d)] (Uddin M et al., 2008)	30.24×10^3
Specific surface area of hydrate particles /(m^2/m^3) (Uddin M et al., 2008)	375×10^3
Activation energy ΔE/(J/mol) (Uddin M et al., 2008)	81084.8
Reaction enthalp ΔH_h/(J/mol) (Jung JW et al., 2010)	58000
CO_2 hydrate thermal conductivity/[W/(m·K)] (Jung JW et al., 2010)	0.49
CO_2 hydrate heat capacity/[J/(kg·K)] (Gharasoo M et al., 2019)	1896.8

3.2.2. Establishment of the anticline structure model

Fig. 6 presents the distribution of the top reservoir layer in anticline structures with varying interlimb angles. According to the literature (Li YB et al., 2024), the interlimb angles of hydrate reservoirs range from 30° to 180°. This study designs four cases with interlimb angles of 180°, 120°, 90°, and 60° to investigate their influence on CO_2 hydrate sequestration.

Fig. 7 illustrates the distribution of initial pressure, temperature and CO_2 hydrate stability zone in anticline structures with varying interlimb angles. In anticline structures, pressure contours exhibit horizontal distribution patterns, governed exclusively by reservoir depth variations. Meanwhile, the temperature contours exhibit a convex arc-shaped distribution, consistent with the geometry of the anticline structure. At the same depth, the central region of the reservoir exhibits a higher temperature, while the wings show lower temperatures. In anticline structures, the lower boundary of the CO_2 hydrate stability zone in the wings shifts downward as the interlimb angle decreases, reflecting the influence of the temperature field on the CO_2 hydrate stability zone.

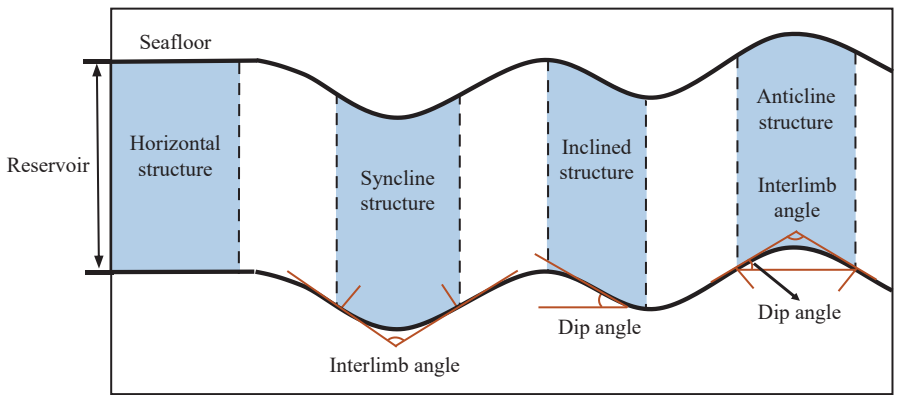

Fig. 3. Different structural types of seafloor reservoirs.

3.2.3. Establishment of the syncline structure model

Fig. 8 represents the distribution of the top reservoir layer in syncline structures with varying interlimb angles. This study designs four cases with interlimb angles of 180°, 120°, 90°, and 60° to examine their impact on CO_2 hydrate sequestration.

Fig. 9 shows the distribution of initial pressure, temperature and CO_2 hydrate stability zone in syncline structures with varying interlimb angles. In syncline structures, the pressure contours are distributed horizontally, while the temperature contours display a concave arc-shaped distribution, following the geometry of the structure. At the same reservoir depth, the temperature at the center of the reservoir is lower, while that at the wings is higher. In anticline structures, the lower boundary of the CO_2 hydrate stability zone at the reservoir wings gradually shifts upward as the interlimb angle decreases.

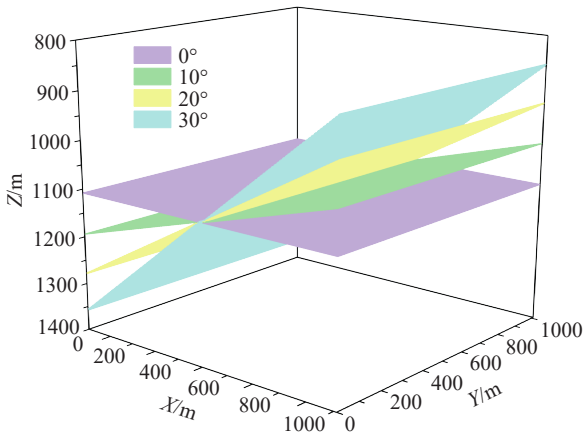

Fig. 4. Distribution of the top reservoir layer in inclined structures with varying dip angles.

4. Results and discussion

4.1. Effect of geological structure on CO_2 hydrate sequestration

In syncline and anticline structures with an interlimb angle of 120°, the dip angle at the wings is 30°. The study investigates the effect of different structures with a 30° dip angle on CO_2 hydrate sequestration, compared with horizontal structures.

4.1.1. Effect of geological structure on CO_2 hydrate formation and conversion rates

Fig. 10 illustrates the CO_2 hydrate formation mass (F_{hyd}) and conversion rate (R_{CO_2}) curves for different geological structures, with R_{CO_2} defined as the percentage of injected CO_2 transformed into hydrates. Although all structures exhibit progressive increases in F_{hyd} over time, their growth patterns diverge markedly. After 500 years, the horizontal structure accumulates 342×10^6 kg of hydrates, serving as the reference case. Compared to this baseline, the inclined, anticline, and syncline structures show variations of −19.12%, +6.60%, and −7.19% in F_{hyd}, respectively. This trend stems from the higher temperatures in the upper section of the inclined structure and the wings of the syncline structure at the same reservoir depth. This inhibits heat exchange between the hydrate formation zone and the surrounding lower temperature reservoir after

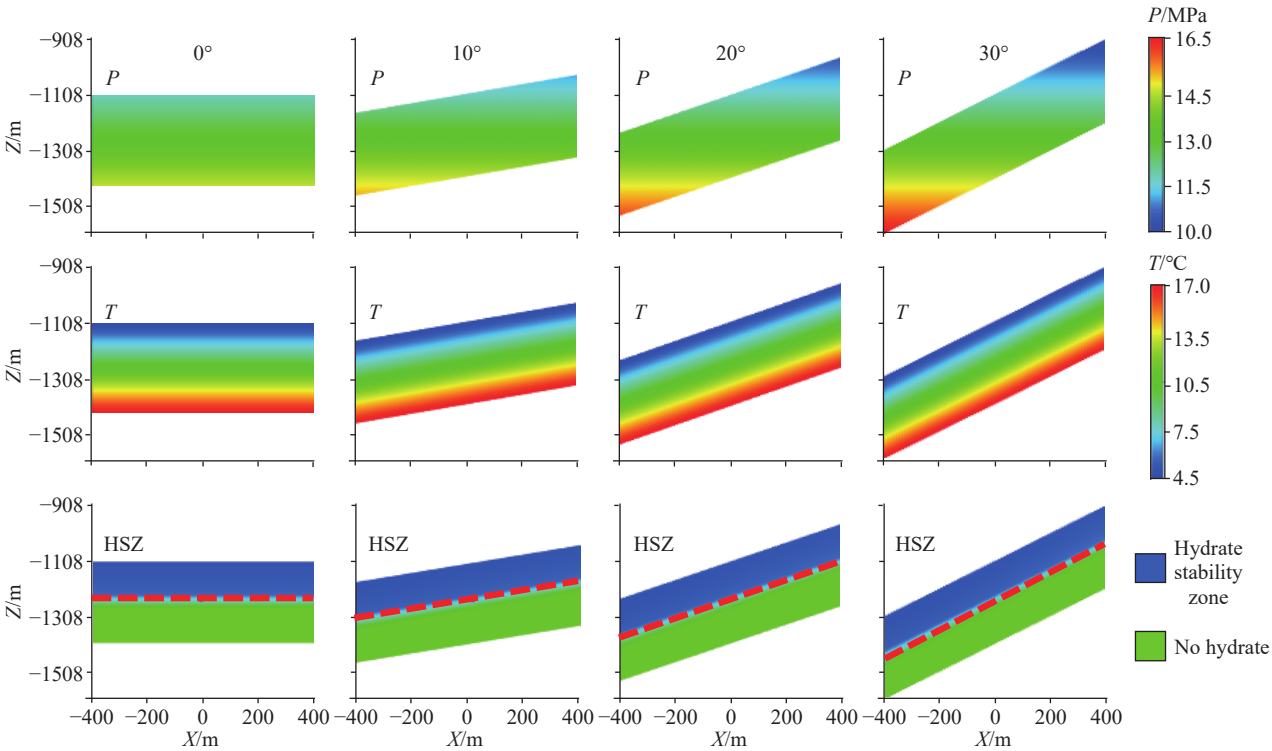

Fig. 5. Distribution of initial pressure, temperature and CO_2 hydrate stability zone in inclined structures with varying dip angles. The red dashed line indicates the lower boundary of the CO_2 hydrate stability zone.

the exothermic formation of hydrates, thereby reducing hydrate formation. Conversely, the lower temperature at the wings of the anticline structure promotes hydrate formation, increasing the amount of hydrate. With the same CO_2 injection amount, the hydrate conversion rates in the horizontal, inclined, anticline, and syncline structures are 9.31%, 7.52%, 9.92%, and 8.63%, respectively. These values of R_{CO_2} demonstrate a direct correlation with F_{hyd} observed in each geological structure.

In summary, geological structures significantly influence CO_2 hydrate formation. At a fixed 30° dip angle, anticline structures demonstrate optimal hydrate formation performance, whereas inclined structures exhibit the lowest efficiency. Thus, for CO_2 sequestration projects aiming to maximize hydrate storage capacity, anticlinal reservoirs should be given top priority in site selection.

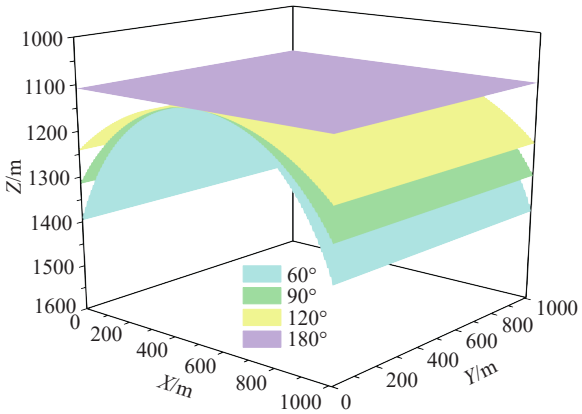

Fig. 6. Distribution of the top reservoir layer in anticline structures with varying interlimb angles.

4.1.2. Effect of geological structure on hydrate sequestration dynamics

The formation of CO_2 hydrates is influenced by factors such as temperature, pressure, permeability, and fluid migration characteristics. Geological structure affects reservoir temperature distribution and CO_2 migration pathways. As a result, the dynamic evolution of hydrate formation varies significantly among different geological structures.

Fig. 11 shows the vertical CO_2 saturation distribution and evolution from the end of injection (10 years) to 500 years across structures. The distribution of liquid CO_2 is significantly affected by geological structures. In the horizontal structure, the CO_2 distribution exhibits an elliptical shape. In the inclined structure, the direction of the ellipse aligns with the dip angle. In the anticline structure, the distribution takes on a convex form, while in the syncline structure, it takes on a concave form. These variations stem from anisotropy in permeability induced by structure. During the injection phase, CO_2 migration is mainly influenced by injection pressure and reservoir permeability. After injection stops, buoyancy becomes the dominant driving force for CO_2 movement across structures (Li SX et al., 2026). In all structures, CO_2 exhibits pronounced vertical migration.

Fig. 12 illustrates the vertical CO_2 hydrate saturation distribution and evolution from the end of injection (10 years) to 500 years across structures. CO_2 hydrate saturation distribution is symmetrical in horizontal structure. When CO_2 migrates upward into the hydrate stability zone via transport driven by buoyancy, only a small amount of hydrate forms initially. This slightly reduces the reservoir's porosity and permeability, but CO_2 continues to rise due to buoyancy.

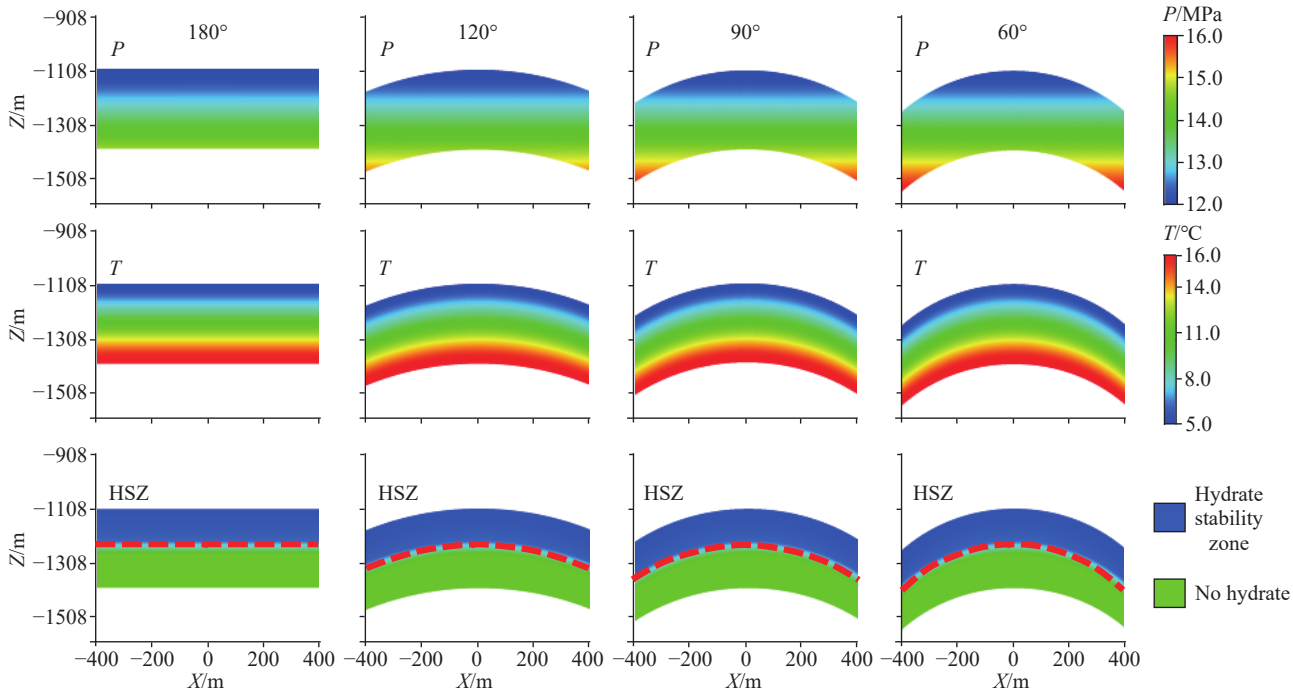

Fig. 7. Distribution of initial pressure, temperature and CO_2 hydrate stability zone in anticline structures with varying interlimb angles. The red dashed line marks the lower boundary of the CO_2 hydrate stability zone.

Since horizontal permeability exceeds vertical permeability, the heat released during hydrate formation dissipates more efficiently through lateral heat transfer. Consequently, hydrates with higher saturation form earlier on both sides of the CO_2 migration path. Ultimately, CO_2 migrates laterally up to 150 m, forming a hydrate cap with a saturation of 0.91 at a depth of 25 m beneath the seafloor.

In the inclined structure, temperature differences lead to distinct CO_2 hydrate formation patterns in the upper and lower sections of the reservoir. At the same depth, the lower section exhibits lower temperatures, which facilitates heat transfer from the hydrate formation zone to the surrounding sediments. This process reduces the temperature at the CO_2 migration front, leading to the early formation of a CO_2 hydrate cap. This cap inhibits both vertical and lateral CO_2 migration in the lower section, while promoting CO_2 into the upper reservoir. Consequently, the lateral migration distance of CO_2 in the lower section is limited to 120 m. In contrast, higher temperatures in the upper section of the inclined structure hindered heat transfer, thereby suppressing the formation of a high-saturation CO_2 hydrate cap. Under the influence of buoyancy, CO_2 continues to migrate upward. Finally, after migrating laterally for 350 m, a hydrate cap with a saturation of 0.95 forms approximately 65 m below the seafloor.

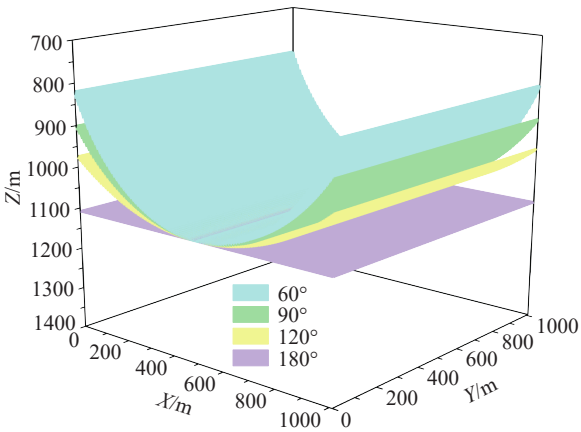

Fig. 8. Distribution of the top reservoir layer in syncline structures with varying interlimb angles.

In the anticline structure, the dynamic evolution of hydrates is similar to that in the horizontal structure, but CO_2 hydrate exhibits a more pronounced convex distribution pattern. This explains that at the same reservoir depth in the anticline structure, the temperature at the wings is lower than at the center. After CO_2 hydrate formation, CO_2 in the wing regions transferred heat more efficiently to the surrounding cooler sediments, causing the temperature to drop below the phase equilibrium temperature and thus promoting hydrate formation. Consequently, a high saturation hydrate cap forms on both sides of the CO_2 migration path in the same timeframe. This process inhibits lateral CO_2 migration and promotes its vertical movement. Ultimately, the lateral migration of CO_2 reaches a maximum distance of 130 m, and a hydrate cap with a saturation of 0.93 forms at approximately 20 m below the seafloor.

In the syncline structure, CO_2 hydrate distribution remains symmetrical, but the convex distribution pattern weakens in the vertical direction. Additionally, the hydrate distribution tends to spread horizontally, with the maximum lateral migration distance increasing to 180 m. This behavior is mainly attributed to the syncline structure, which leads to higher temperatures at the wings at the same depth, thereby

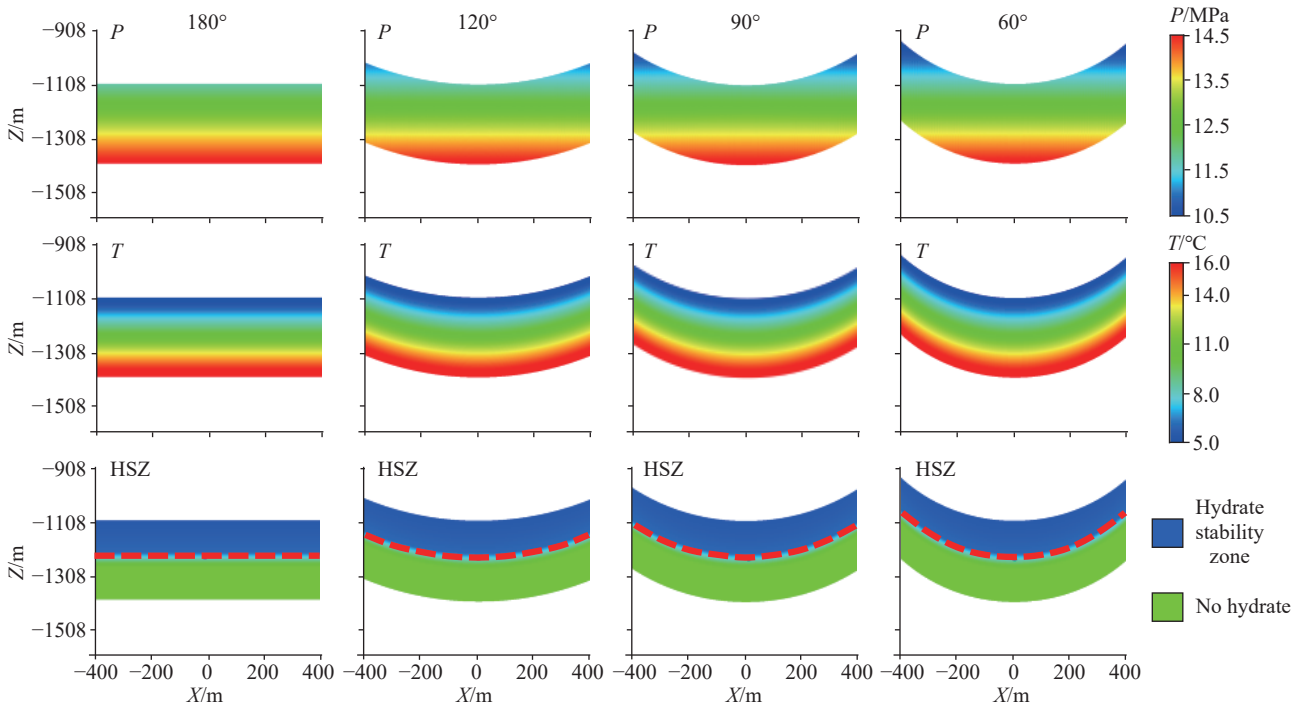

Fig. 9. Distribution of initial pressure, temperature and CO_2 hydrate stability zone in syncline structures with varying interlimb angles. The red dashed line represents the lower boundary of the CO_2 hydrate stability zone.

enhancing the buoyancy of CO_2 migration. The heat released during hydrate formation was transferred less efficiently, preventing the CO_2 temperature from decreasing. As a result, the amount of hydrate formed decreased, the reduction in reservoir permeability slowed, and CO_2 continued to migrate upward under buoyancy forces. Consequently, the migration rate at the wings increases, resulting in a larger lateral extent and reduced vertical migration. Ultimately, a hydrate cap with a saturation of 0.97 forms at approximately 30 m below the seafloor.

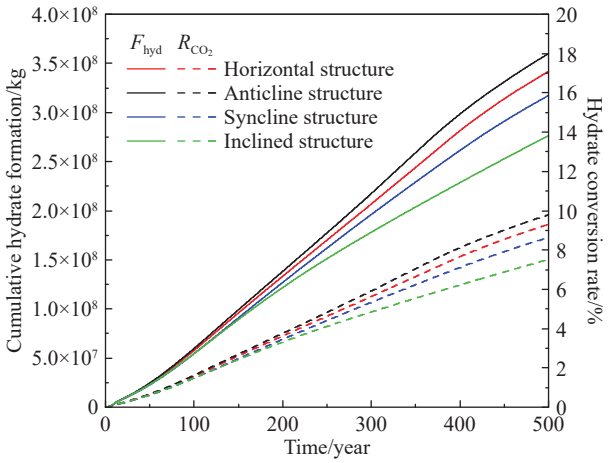

Fig. 10. CO_2 hydrate formation and conversion rate curves for different geological structures.

At the same injection depth and injection volume, CO_2 hydrate distribution varies across different structures. However, in all cases, CO_2 is sequestered within the hydrate cap in the sediment, with no leakage occurring. From the above analysis, it can be concluded that the temperature variation across geological structures is a key factor influencing the amount of CO_2 hydrate formation. Under the same pressure conditions, a greater temperature difference provides a stronger thermodynamic driving force for hydrate formation, allowing more heat to be released and transferred. The safety of CO_2 hydrate sequestration is primarily related to the permeability of the reservoir, while the amount of hydrate formed further affects the reservoir's permeability.

Fig. 13 illustrates the vertical temperature distribution and evolution from the end of injection (10 years) to 500 years across structures. After the end of liquid CO_2 injection, a low-temperature zone forms below the injection point of the vertical well, while a high-temperature zone develops above it. This occurs because the injected liquid CO_2 has the same temperature with the reservoir formation. After CO_2 injection ends, upward CO_2 migration leads to the gradual dissipation of the underlying low-temperature zone. During CO_2 upward migration driven by buoyancy, CO_2 continuously exchanged

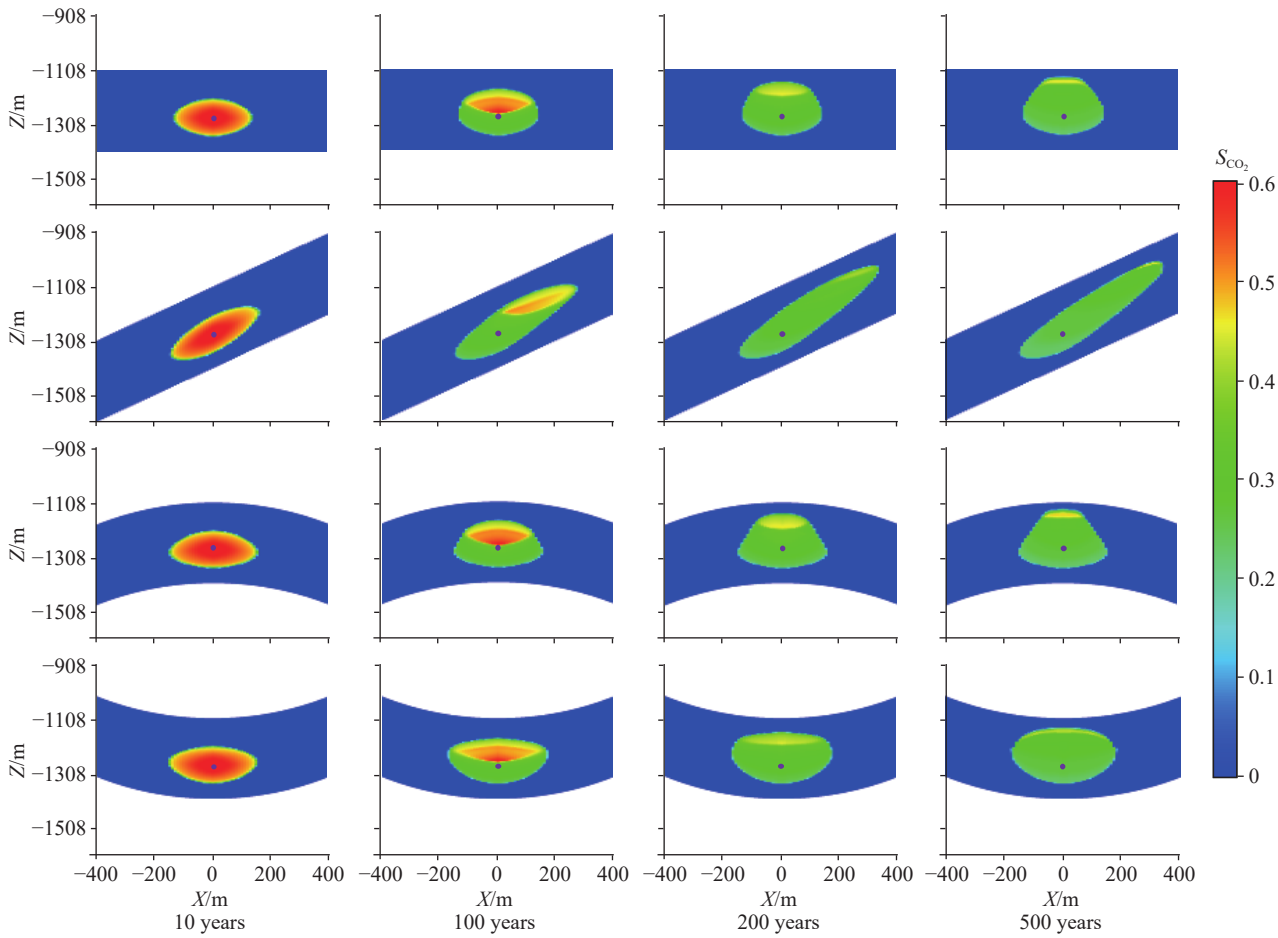

Fig. 11. Vertical CO_2 saturation (S_{CO_2}) distribution and evolution from the end of injection (10 years) to 500 years across structures. The purple dots represent the CO_2 injection points.

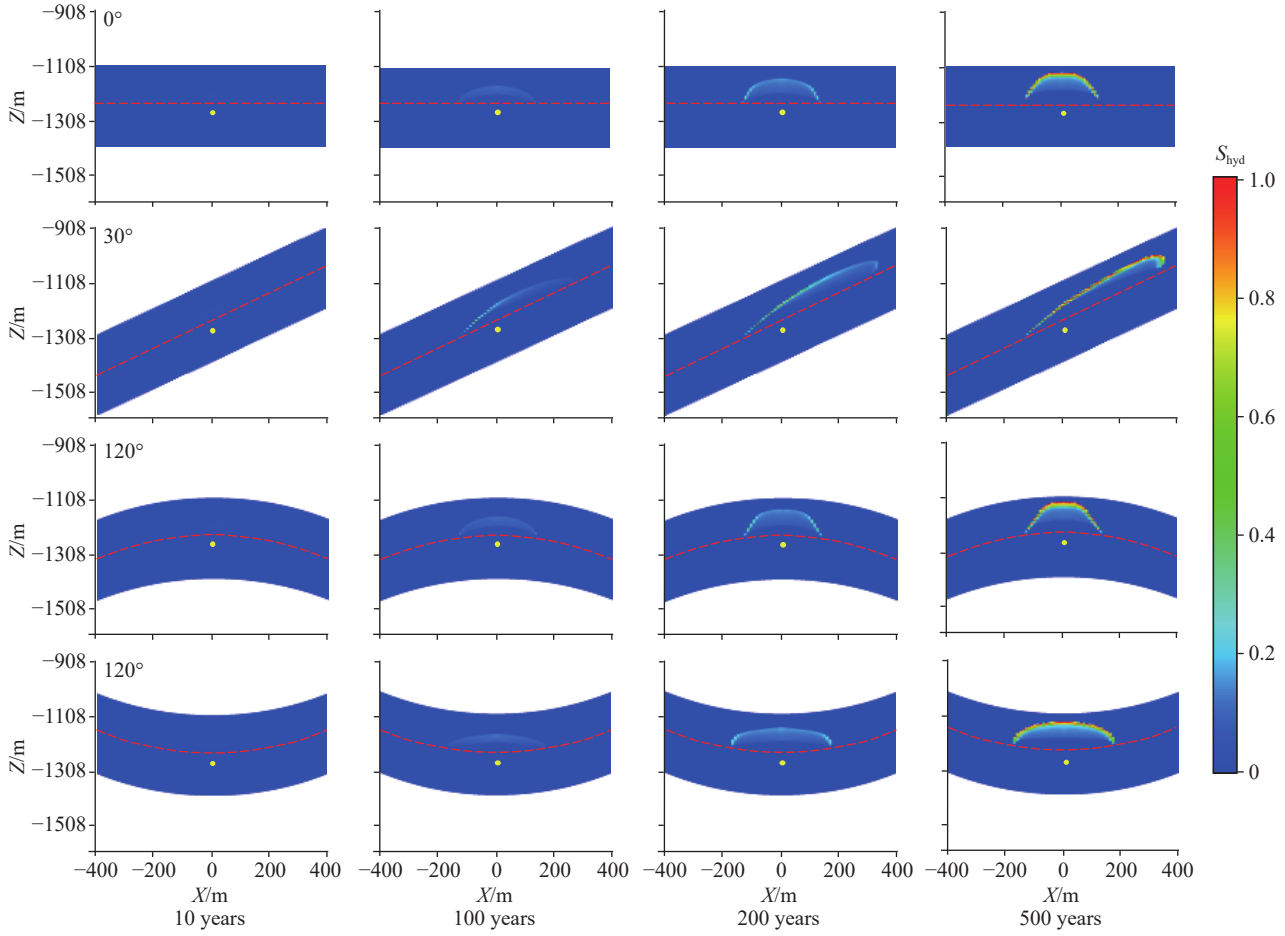

Fig. 12. Vertical CO_2 hydrate saturation (S_{hyd}) distribution and evolution from the end of injection (10 years) to 500 years across structures. The red dashed line marks the lower boundary of the CO_2 hydrate stability zone, and the yellow dots indicate the injection points.

heat with the surrounding reservoir. When CO_2 reaches the lower boundary of the hydrate stability zone, its temperature attains thermal equilibrium with that of the reservoir. As CO_2 enters the hydrate stability zone, exothermic hydrate formation occurs through reaction with pore water, elevating local reservoir temperatures to the phase equilibrium temperature of approximately 10.4 °C (Nole M et al., 2025). The temperature increase within the CO_2 hydrate stability zone is solely attributable to hydrate formation.

Fig. 14 displays the vertical permeability distribution and evolution from the end of injection (10 years) to 500 years across structures. Permeability reduction exhibits a positive correlation with hydrate saturation, attributable to pore space occupation by CO_2 hydrate formation. Within the hydrate stability zone, increasing hydrate saturation directly reduces reservoir permeability (Mahabadi N et al., 2019). Furthermore, localized temperature-pressure variations cause spatial heterogeneity in hydrate formation, resulting in non-uniform permeability reduction. These permeability changes, combined with buoyancy effects, ultimately alters CO_2 migration pathways and affects hydrate distribution patterns.

In summary, all geological structures successfully trap CO_2 beneath impermeable hydrate caps with no observed seafloor leakage. The horizontal structure serves as the baseline case, with the hydrate cap located 25 m below the seafloor and CO_2 migrating up to 150 m laterally. When comparing structures with 30° dip angles to this horizontal reference, the inclined structure shows the most significant changes, increasing the distance from the top of the CO_2 hydrate cap to the seafloor by 160% and lateral migration by 133.33%. In contrast, the anticline structure reduces these metrics by 20% and 13.33% respectively, while the syncline structure increases both by 20%. If the distance is maintained at 25 m, as in the horizontal base model, the inclined and synclinal structures could sequester an additional 730×10^3 t and 360×10^3 t of CO_2, respectively. In contrast, the anticlinal structure would reduce the amount of CO_2 injected by 360×10^3 t. From a safety perspective that prioritizes maximizing the distance between hydrate caps and the seafloor, the inclined structure emerges as the most favorable configuration for CO_2 sequestration.

4.2. Effect of structural dip angle on CO_2 hydrate sequestration

This section investigates the effect of structural dip angle on CO_2 hydrate sequestration by analyzing inclined structures with dip angles of 0°, 10°, 20°, and 30°, and anticline and syncline structures with interlimb angles of 180°, 120°, 90°, and 60°, respectively. The models with a 0° dip angle for the

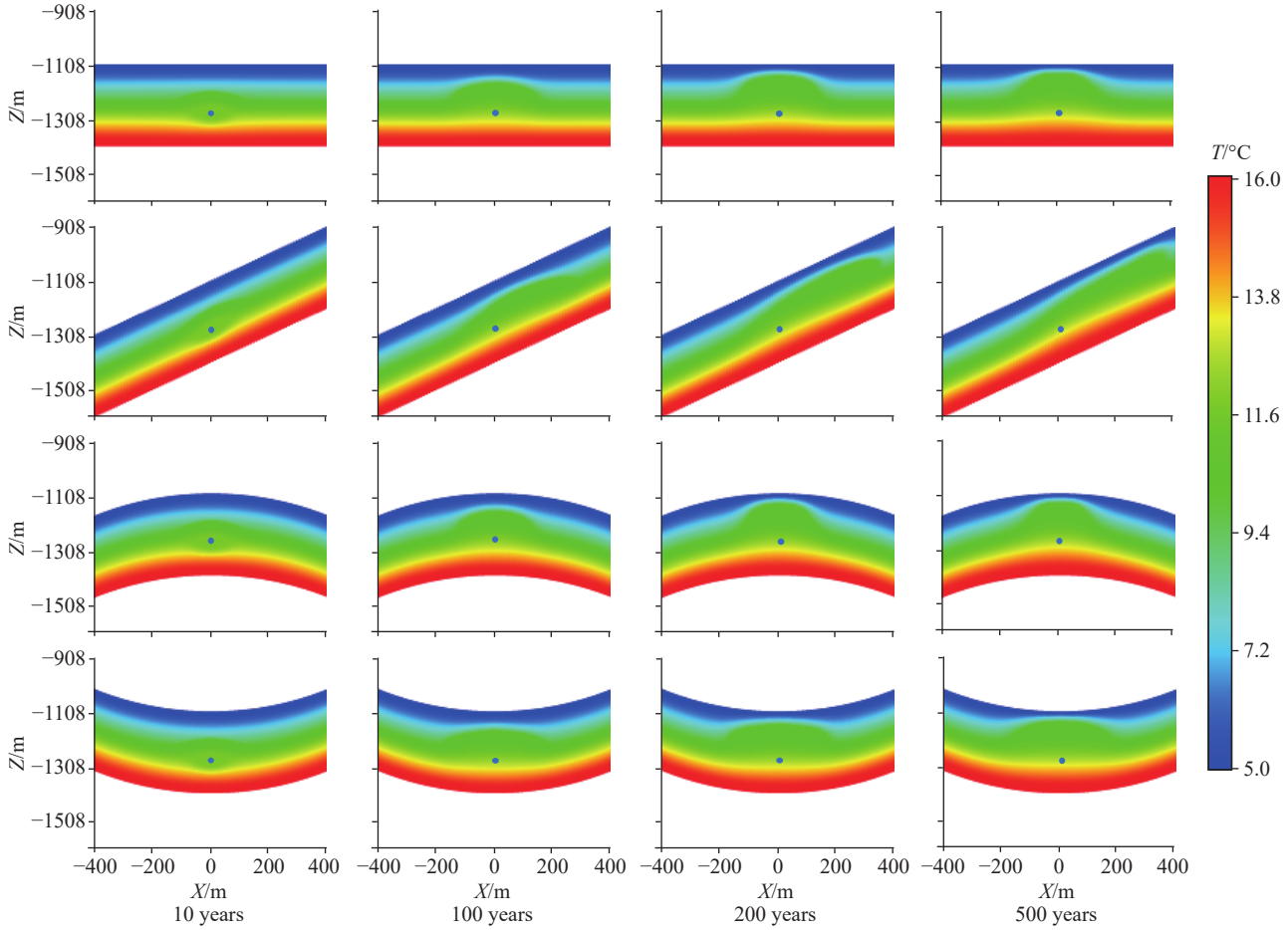

Fig. 13. Vertical temperature (T) distribution and evolution from the end of injection (10 years) to 500 years across structures. The blue dots indicate the location of CO_2 injection.

inclined structure and interlimb angle of 180° for the anticline and syncline structures are the baseline horizontal models.

4.2.1. Effect of structural dip angle on CO_2 hydrate formation and conversion rates

Fig. 15 illustrates the CO_2 hydrate formation mass (F_{hyd}) and conversion rate (R_{CO_2}) curves for inclined structures in different dip angles. During the initial 150 years, dip angle exhibits negligible influence on hydrate formation. After 150 years, as the dip angle increases, hydrate formation mass decreases significantly. Specifically, compared to the horizontal structure, which forms 342×10^6 kg of hydrate, inclined structures with dip angles of 10°, 20°, and 30° show decreases of 3.74%, 12.50%, and 19.12%, respectively. The CO_2 conversion rate is directly related to hydrate formation mass. This trend can be explained by the fact that CO_2 continues to migrate upward and laterally due to buoyancy after 150 years. The larger the dip angle, the greater the migration distance. However, a larger dip angle also leads to higher temperatures in the upper section of the inclined structure at the same depth, which inhibits hydrate formation. Consequently, the larger dip angle, the lesser amount of hydrate formation.

Fig. 16 presents the CO_2 hydrate formation mass (F_{hyd}) and conversion rate (R_{CO_2}) curves for different interlimb angles in anticline structures. After 150 years, the amount of CO_2 hydrate formed increases gradually as the interlimb angle decreases. Specifically, relative to the horizontal structure, the amount of hydrate formed increases by 6.60%, 9.03%, and 10.54% in anticline structures with interlimb angles of 120°, 90°, and 60°, respectively. The CO_2 conversion rate is directly proportional to the amount of hydrate formed. This behavior results from the anticline structure causing a gradual temperature decrease at the wings of the structure at the same reservoir depth as the interlimb angle decreases. This temperature decrease enhances heat exchange between the hydrate formation zone and the surrounding reservoir. Consequently, as the interlimb angle decreases, hydrate formation mass increases.

Fig. 17 illustrates the CO_2 hydrate formation (F_{hyd}) and conversion rate (R_{CO_2}) curves for different interlimb angles in syncline structures. After 100 years, hydrate formation mass gradually decreases as the interlimb angle reduces. Specifically, compared to the horizontal structure, the hydrate formation in syncline structures with interlimb angles of 120°, 90°, and 60° decrease by 7.19%, 10.33%, and 12.57%, respectively. The CO_2 conversion rate is directly proportional to hydrate formation mass. This occurs because the syncline structure causes the temperature at both wings to increase as the interlimb angle decreases at the same reservoir depth, which hinders heat exchange between the hydrate formation zone and the surrounding reservoir. Consequently, as the

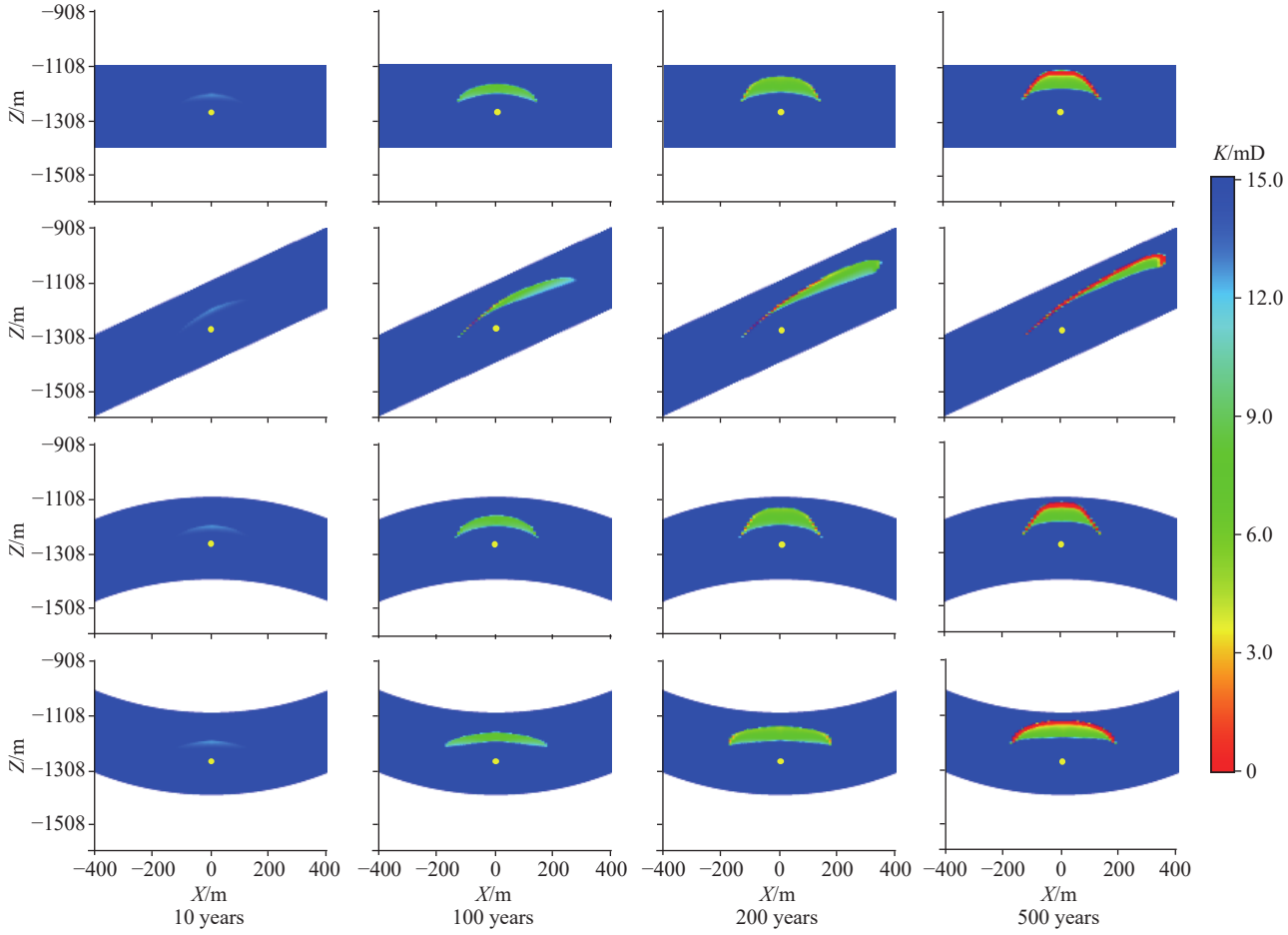

Fig. 14. Vertical permeability (K) distribution and evolution from the end of injection (10 years) to 500 years across structures. The yellow dots denote the CO_2 injection points.

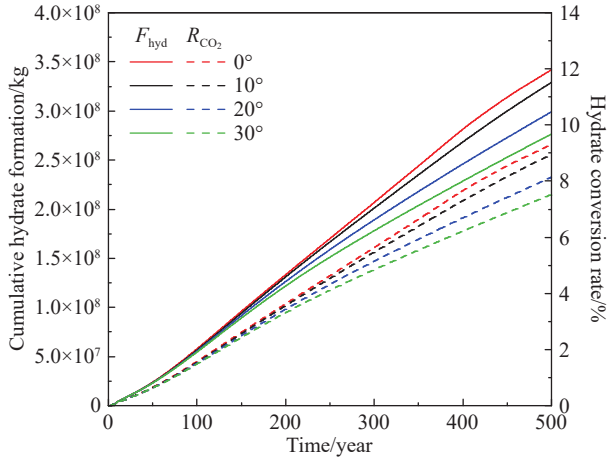

Fig. 15. CO_2 hydrate formation mass and conversion rate curves for inclined structures in different dip angles.

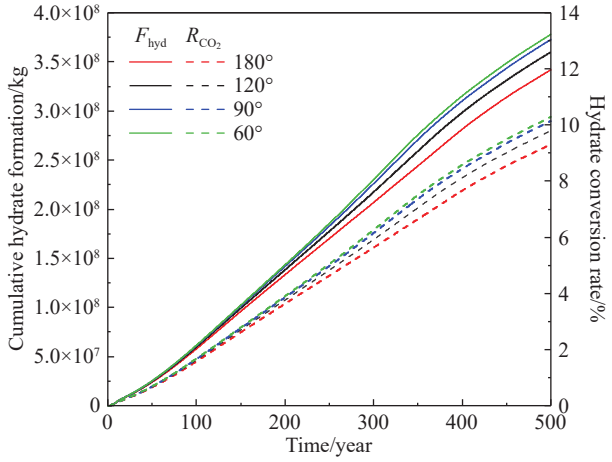

Fig. 16. CO_2 hydrate formation mass and conversion rate curves for different interlimb angles in anticline structures.

interlimb angle of the syncline structure decreases, hydrate formation mass gradually reduces.

4.2.2. Effect of structural dip angle on the dynamic evolution of hydrate sequestration

Fig. 18 shows the vertical distribution and evolution of CO_2 hydrate saturation from the end of injection (10 years) to 500 years in inclined structures with different dip angles. After 100 years, high-saturation hydrate caps emerge at the CO_2 migration front within the reservoir's lower section. As dip angles increase, these hydrate caps gradually shift toward the center position of the reservoir plane due to thermally favorable conditions. Specifically, larger dip angles induce lower temperatures at the lower section of the reservoir at the same depth, which promotes preferential hydrate formation closer to the center of the plane at the 0 m position.

Over time, all inclined structures develop a highly saturated hydrate cap at a specific depth below the seafloor, without any CO_2 leakage. In inclined reservoirs with dip angles of 10°, 20°, and 30°, the lateral extent of hydrate formation in the upper section increases by 26.67%, 86.67%, and 133.33%, respectively, compared to the 150 m observed in horizontal structures. The distance from the top of hydrate cap to the seafloor increases by 20%, 80%, and 160%, respectively, compared to the 25 m depth in horizontal structures. This trend is attributed to higher temperatures in the upper section of the inclined structure as the dip angle rises at the same reservoir depth, which promotes the migration of liquid CO_2 to the upper section of the reservoir under the influence of buoyancy. As CO_2 migrates, the area of hydrate formation increases. However, as accumulating hydrates deplete the mobile CO_2 beneath the cap, the buoyant driving force progressively weakens, increasing the distance from the hydrate cap to the seafloor. Ultimately, the CO_2 sequestration capacity in the upper section of reservoirs with dip angles of 10°, 20°, and 30° increases by 34.00%, 45.82%, and 50.78%, respectively, compared to 547×10^3 t in horizontal structures. In summary, as the dip angle increases, the lateral extent of CO_2 migration increases, and the distance from the top of the CO_2 hydrate cap to the seafloor grows.

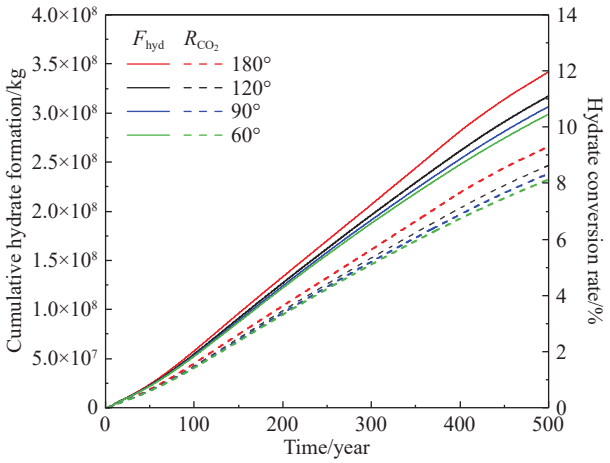

Fig. 17. CO_2 hydrate formation mass and conversion rate curves for different interlimb angles in syncline structures.

Fig. 19 illustrates the vertical distribution and evolution of CO_2 hydrate saturation from the end of injection (10 years) to 500 years in anticline structures with different interlimb angles. After 200 years, as the interlimb angle decreases, the convex distribution of CO_2 hydrate becomes more pronounced. The anticline structure causes the temperature at the wings to reduce with a decreasing interlimb angle at the same reservoir depth. This temperature decrease facilitates the formation of CO_2 hydrates at the wings, where reduced permeability hinders lateral CO_2 migration, causing more CO_2

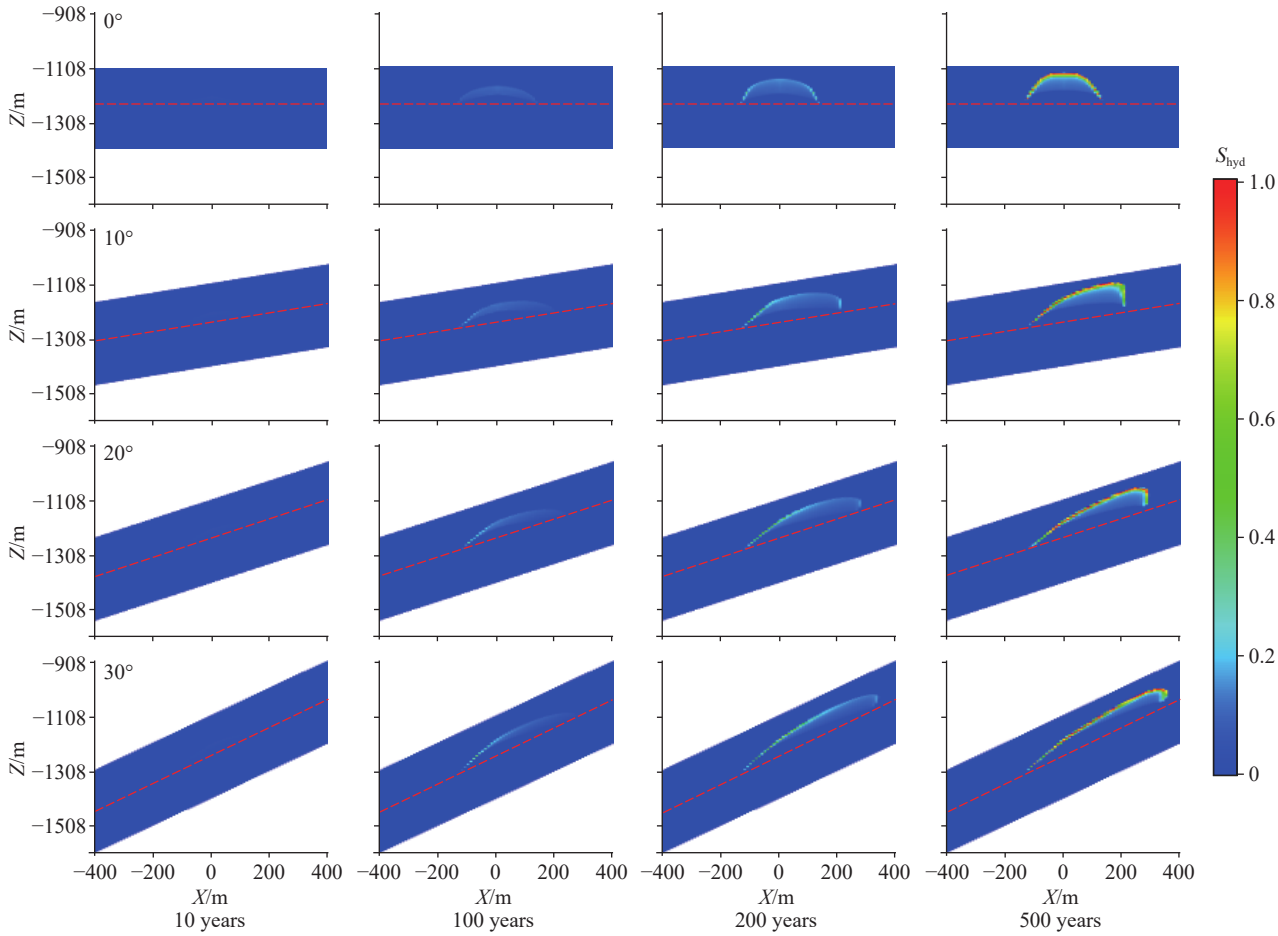

Fig. 18. Vertical distribution and evolution of CO_2 hydrate saturation from the end of injection (10 years) to 500 years in inclined structures with different dip angles.

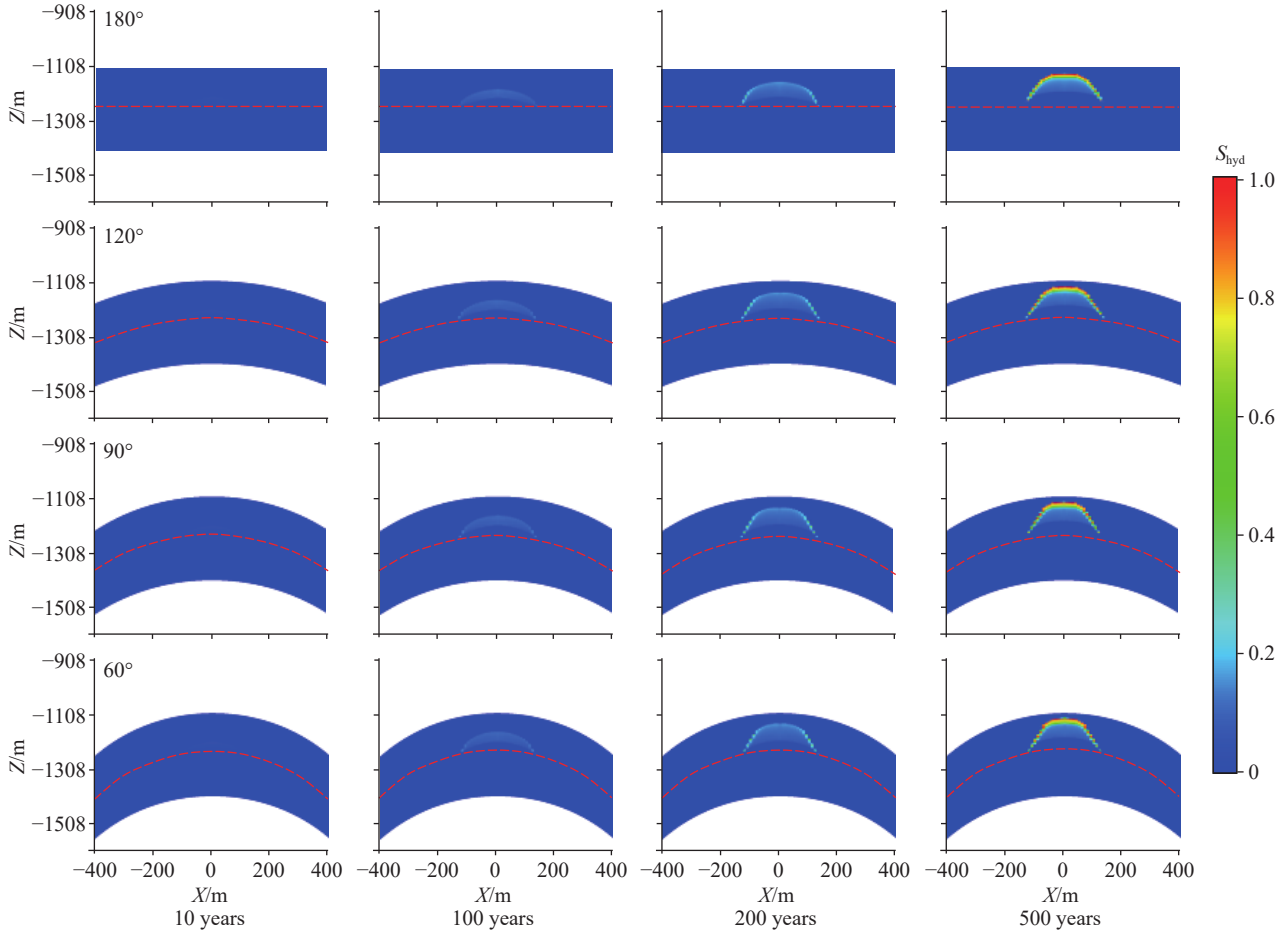

Fig. 19. Vertical distribution and evolution of CO_2 hydrate saturation from the end of injection (10 years) to 500 years in anticline structures with different interlimb angles.

to migrate upward due to buoyancy. Ultimately, this results in the low-permeability hydrate cap being positioned closer to the seafloor. Compared to the horizontal structure, the distance from the top of hydrate cap to the seafloor decreases by 20%, 32%, and 40% for anticline structures with interlimb angles of 120°, 90°, and 60°, respectively.

Fig. 20 presents the vertical distribution and evolution of CO_2 hydrate saturation from the end of injection (10 years) to 500 years in syncline structures with different interlimb angles. With the reduction in the interlimb angle after 200 years, the lateral extent of hydrate formation increases. The high-saturation hydrate cap transitions from a convex shape to nearly horizontal. This trend is driven by rising temperatures at the reservoir wings at the same depth, as the interlimb angle decreases. As a result, the density difference between CO_2 and water increases, thereby enhancing the buoyant force acting on CO_2, promoting its lateral migration along the wings, expanding its horizontal spread, and constraining vertical development. Compared to the horizontal structure, the distance between the top of hydrate cap and the seafloor increases by 20%, 36%, and 40% in syncline structures with interlimb angles of 120°, 90°, and 60°, respectively. In summary, a smaller interlimb angle in syncline structures results in a flatter hydrate cap and a greater distance between the top of hydrate cap and the seafloor.

5. Conclusions

This study establishes four geological structure models: Horizontal, inclined, anticline, and syncline. It investigates the dynamic evolution of key physical fields including CO_2 saturation, CO_2 hydrate saturation, temperature, and permeability, as well as the hydrate formation mass across these structures. The main conclusions drawn are as follows.

(i) The geological structure significantly influences both the hydrate formation mass and the vertical distance between the top of the hydrate cap and the seafloor. Compared to the horizontal structure, reservoirs with a 30° dip angle exhibit changes in CO_2 hydrate formation mass of −19.12%, +6.60%, and −7.19% for the inclined, anticline, and syncline structures, respectively. The corresponding distance changes are +160%, −20%, and +20%, respectively. The temperature variation across geological structures is a key factor influencing the amount of CO_2 hydrate formation, while permeability is a major factor affecting the safety of CO_2 sequestration.

(ii) The structural dip angle influences the amount of CO_2 hydrate formation. Compared to the horizontal structure, hydrate formation mass in inclined structures with dip angles of 10°, 20°, and 30° decreases by 3.74%, 12.50%, and 19.12%, respectively. Hydrate formation mass increases by 6.60%, 9.03%, and 10.54% in anticline structures with 120°,

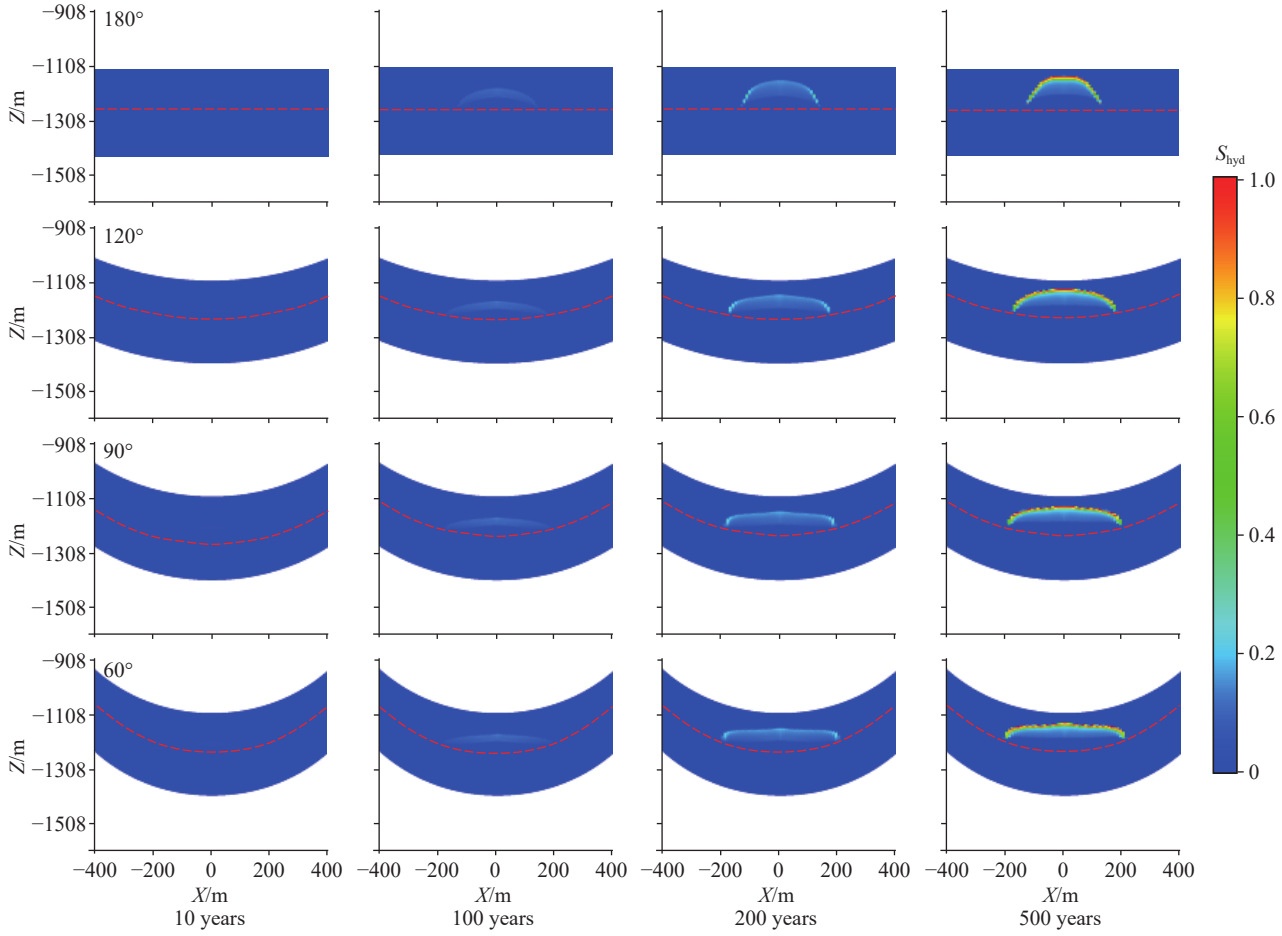

Fig. 20. Vertical distribution and evolution of CO_2 hydrate saturation from the end of injection (10 years) to 500 years in syncline structures with different interlimb angles.

90°, and 60° interlimb angles, respectively. In syncline structures with the same interlimb angles, it decreases by 7.19%, 10.33%, and 12.57%, respectively. Anticline structures promote hydrate formation, while inclined and syncline structures inhibit it.

(iii) The structural dip angle influences the dynamic evolution of CO_2 hydrate formation. As the dip angle increases, different geological structures exhibit distinct evolutionary patterns. In inclined structures, the lateral extent of CO_2 migration in the upper section expands, and the hydrate cap moves farther from the seafloor. In anticline structures, the convex shape distribution becomes more pronounced, and the hydrate cap is closer to the seafloor. In syncline structures, the distribution pattern transitions from a convex shape to a horizontal form, and the distance between the top of the hydrate cap and the seafloor increases.

(iv) Geological structures have a significant impact on CO_2 hydrate sequestration. If maximizing the amount of hydrate formation is the primary objective, the anticline structure is the most favorable. Conversely, if the goal is to increase the vertical distance between the top of the hydrate cap and the seafloor, the inclined structure is the most suitable reservoir. Geological factors such as structure type, seafloor depth, and reservoir heterogeneity in different marine environments can affect hydrate formation mass, stability, and CO_2 migration pathways. Therefore, although the current results provide valuable guidance for selecting promising sedimentary structures, further investigation of the target reservoirs is necessary before large-scale CO_2 hydrate sequestration in marine sediments.

CRediT authorship contribution statement

Shu-xia Li conceived the presented idea and reviewed the manuscript. Zhong-xue Song wrote the original draft, developed the methodology, and designed the research. Yang Guo and Gao-wei Hu reviewed and edited the manuscript. Lu Liu and Ben-kui Lou were responsible for data curation and formal analysis. Hao Sun, Jun-hao Liu, and Zhen-hao Ren conducted the investigation and validation. All authors provided feedback on the research, analysis, and manuscript.

Declaration of competing interest

The authors declare no conflicts of interest.

Acknowledgement

The work is supported by the National Natural Science Foundation of China (U24A20612) and the National Key R&D Program of China (2021YFC2800903), which are gratefully acknowledged. In addition, the authors thank the anonymous reviewers for their professional suggestions in improving this manuscript.

References

Adams EE, Caldeira K. 2008. Ocean storage of CO_2. Elements, 4(5), 319–324. doi: 10.2113/gselements.4.5.319.

Akai T, Saito N, Hiyama M, Okabe H. 2021. Numerical modelling on CO_2 storage capacity in depleted gas reservoirs. Energies, 14(13), 3978. doi: 10.3390/en14133978.

Aminu MD, Nabavi SA, Rochelle CA, Manovic V. 2017. A review of developments in carbon dioxide storage. Applied Energy, 208, 1389–1419. doi: 10.1016/j.apenergy.2017.09.015.

Almenningen S, Betlem P, Hussain A, Roy S, Senger K, Ersland G. 2019. Demonstrating the potential of CO_2 hydrate self-sealing in Svalbard, Arctic Norway. International Journal of Greenhouse Gas Control, 89, 1–8. doi: 10.1016/j.ijggc.2019.06.010.

Boswell R, Shelander D, Lee M, Latham T, Collett T, Guerin G, Moridis G, Reagan M, Goldberg D. 2009. Occurrence of gas hydrate in Oligocene Frio sand: Alaminos canyon block 818: Northern Gulf of Mexico. Marine and Petroleum Geology, 26(8), 1499–1512. doi: 10.1016/j.marpetgeo.2009.03.005.

Cao XW, Wang HC, Yang KR, Wu SC, Chen Q, Bian J. 2022. Hydrate-based CO_2 sequestration technology: Feasibilities, mechanisms, influencing factors, and applications. Journal of Petroleum Science and Engineering, 219, 111121. doi: 10.1016/j.petrol.2022.111121.

Carman PC. 1997. Fluid flow through granular beds. Chemical Engineering Research and Design, 75, S32–S48. doi: 10.1016/s0263-8762(97)80003-2.

Chen HN, Sun YF, Cao BJ, Wang ML, Wang M, Zhong JR, Sun CY, Chen GJ. 2024. Enhanced gas production and CO_2 storage in hydrate-bearing sediments via pre-depressurization and rapid CO_2 injection. Chinese Journal of Chemical Engineering, 67, 126–134. doi: 10.1016/j.cjche.2023.09.016.

Collett TS, Boswell R, Waite WF, Kumar P, Roy SK, Chopra K, Singh SK, Yamada Y, Tenma N, Pohlman J, Zyrianova M. 2019. India national gas hydrate program expedition 02 summary of scientific results: Gas hydrate systems along the eastern continental margin of India. Marine and Petroleum Geology, 108, 39–142. doi: 10.1016/j.marpetgeo.2019.05.023.

Cui JL, Sun ZF, Kan JY, Jia S, Sun CY, Chen GJ, Wang XH, Yuan Q, Li N. 2021. Study on the factors affecting the sealing performance and mechanical stability of CO_2 hydrate cap during gas production from methane hydrate. Journal of Natural Gas Science and Engineering, 93, 104050. doi: 10.1016/j.jngse.2021.104050.

Dai S, Kim J, Xu Y, Waite WF, Jang J, Yoneda J, Collett TS, Kumar P. 2019. Permeability anisotropy and relative permeability in sediments from the national gas hydrate program expedition 02, offshore India. Marine and Petroleum Geology, 108, 705–713. doi: 10.1016/j.marpetgeo.2018.08.016.

Dai ZX, Zhang Y, Stauffer P, Xiao T, Zhang MK, Ampomah W, Yang CB, Zhou YQ, Ding M, Middleton R, Soltanian MR, Bielicki Jeffrey M. 2017. Injectivity evaluation for offshore CO_2 sequestration in marine sediments. Energy Procedia, 114, 2921–2932. doi: 10.1016/j.egypro.2017.03.1420.

Dehghani MR, Kafi M, Nikravesh H, Aghel M, Mohammadian E, Kazemzadeh Y, Azin R. 2024. Data driven models for predicting pH of CO_2 in aqueous solutions: Implications for CO_2 sequestration. Results in Engineering, 24, 102889. doi: 10.1016/j.rineng.2024.102889.

Gharasoo M, Babaei M, Haeckel M. 2019. Simulating the chemical kinetics of CO_2-methane exchange in hydrate. Journal of Natural Gas Science and Engineering, 62, 330–339. doi: 10.1016/j.jngse.2018.12.018.

Gu YH, Liu XJ, Li Y, Lu HF, Xu CL, Ren JF, Chen GJ, Linga P, Zhao JZ, Yin ZY. 2025. Feasibility analysis of liquid CO_2 injection and sequestration as hydrates in south China sea marine sediments over 100 years. Applied Energy, 380, 125068. doi: 10.1016/j.apenergy.2024.125068.

Guo Y, Li SX, Sun H, Wu DD, Liu L, Zhang NT, Qin XW, Lu C. 2024. Enhancing gas production and CO_2 sequestration from marine hydrate reservoirs through optimized CO_2 hydrate cap. Energy, 303, 131821. doi: 10.1016/j.energy.2024.131821.

House KZ, Schrag DP, Harvey CF, Lackner KS. 2006. Permanent carbon dioxide storage in deep-sea sediments. Proceedings of the National Academy of Sciences of the United States of America, 103(33), 12291–12295. doi: 10.1073/pnas.0605318103.

Imaoka T, Tobase T, Sato T, Shigeoka Y. 2024. Feasibility of CO_2 hydrate storage in sub-seabed sediments of the Sea of Japan and the Pacific Ocean around Japan. Proceedings of the 17th Greenhouse Gas Control Technologies Conference (GHGT-17). doi:10.2139/ssrn.5065339.

Izadpanahi A, Blunt MJ, Kumar N, Ali M, Tassinari CCG, Sampaio MA. 2024. A review of carbon storage in saline aquifers: Mechanisms, prerequisites, and key considerations. Fuel, 369, 131744. doi: 10.1016/j.fuel.2024.131744.

Jia SJ, Yang LB, Han Y, Zhang TF, Zhang XW, Gong PY, Du SY, Chen Y, Ding JB. 2024. Rapid growth of CO_2 hydrate as a promising way to mitigate the greenhouse effect. Materials Today Physics, 48, 101548. doi: 10.1016/j.mtphys.2024.101548.

Jing J, Yang YL, Cheng JM, Ding ZJ, Wang DD, Jing XW. 2023. Analysis of the effect of formation dip angle and injection pressure on the injectivity and migration of CO_2 during storage. Energy, 280, 128021. doi: 10.1016/j.energy.2023.128021.

Jung JW, Espinoza DN, Santamarina JC. 2010. Properties and phenomena relevant to CH_4-CO_2 replacement in hydrate-bearing sediments. Journal of Geophysical Research: Solid Earth, 115(B10), 2009JB000812. doi: 10.1029/2009JB000812.

Yamaguchi AJ, Sato T, Tobase T, Wei XR, Huang L, Zhang J, Bian J, Liu TY. 2023. Multiscale numerical simulation of CO_2 hydrate storage using machine learning. Fuel, 334, 126678. doi: 10.1016/j.fuel.2022.126678.

Kim HC, Bishnoi PR, Heidemann RA, Rizvi SSH. 1987. Kinetics of methane hydrate decomposition. Chemical Engineering Science, 42(7), 1645–1653. doi: 10.1016/0009-2509(87)80169-0.

Kim HS, Cho GC. 2019. Experimental simulation of the self-trapping mechanism for CO_2 sequestration into marine sediments. Minerals, 9(10), 579. doi: 10.3390/min9100579.

Kuang NJ, Zhou JP, Xian XF, Zhang CP, Yang K, Dong ZQ. 2023. Geomechanical risk and mechanism analysis of CO_2 sequestration in unconventional coal seams and shale gas reservoirs. Rock Mechanics Bulletin, 2(4), 100079. doi: 10.1016/j.rockmb.2023.100079.

Kumar Y, Sangwai JS. 2023. Environmentally sustainable large-scale CO_2 sequestration through hydrates in offshore basins: Ab initio comprehensive analysis of subsea parameters and economic perspective. Energy & Fuels, 37(13), 8739–8764. doi: 10.1021/acs.energyfuels.3c00581.

Lou BK, Li SX, Sun H, Liu L, Guo Y. 2025. Study on the factors influencing CO_2 hydrate sequestration in CH_4 hydrate-bearing reservoirs. Energy, 323, 135777. doi: 10.1016/j.energy.2025.135777.

Li N, Kan JY, Sun CY, Chen GJ. 2022. Hydrate formation from liquid CO_2 in a glass beads bed. Chinese Journal of Chemical Engineering, 43, 185–191. doi: 10.1016/j.cjche.2022.01.008.

Li SX, Wu DD, Wang XP, Hao YM. 2021. Enhanced gas production from marine hydrate reservoirs by hydraulic fracturing assisted with sealing burdens. Energy, 232, 120889. doi: 10.1016/j.energy.2021.120889.

Li SX, Lou BK, Hu GW, Bu QT, Song ZX, Liu L, Guo Y. 2026. Quantifying CO_2 hydrate sequestration: A multi-physics simulation of megatonne-scale transport and millennial-scale trapping dynamics. Fuel, 408, 137680. doi: 10.1016/j.fuel.2025.137680.

Li YB, Xu TF, Xin X, Zang YQ, Yu H, Zhu HX, Yuan YL. 2024. Effects of dipping and folded structure on gas production from hydrate-bearing sediments. SPE Journal, 29(2), 1129–1146. doi: 10.2118/217991-pa.

Li ZW, Dong MZ, Li SL, Huang S. 2006. CO_2 sequestration in depleted oil and gas reservoirs —caprock characterization and storage capacity. Energy Conversion and Management, 47(11–12), 1372–1382. doi: 10.1016/j.enconman.2005.08.023.

Ling ZY, Pan JY, Kontchouo FMB, Liu SS, Lu XJ, Guo X, Penzik MV, Kozlov AN, Huang Y, Zhang S. 2024. Current situation of marine CO_2 sequestration and analysis of related environmental issues. Fuel, 366, 131288. doi: 10.1016/j.fuel.2024.131288.

Liu SQ, Liu T, Zheng SJ, Wang R, Sang SX. 2023. Evaluation of carbon dioxide geological sequestration potential in coal mining area. International Journal of Greenhouse Gas Control, 122, 103814. doi: 10.1016/j.ijggc.2022.103814.

Liu Z, Xu JC, Li HY, Li SX, Fan XW. 2023. Numerical investigation of CO_2 storage capacity via hydrate in deep-sea sediments. Energy & Fuels, 37(23), 18996–19010. doi: 10.1021/acs.energyfuels.3c03196.

Luo A, Li YM, Chen X, Zhu ZY, Peng Y. 2022. Review of CO_2 sequestration mechanism in saline aquifers. Natural Gas Industry B, 9(4), 383–393. doi: 10.1016/j.ngib.2022.07.002.

Mahabadi N, Dai S, Seol Y, Jang J. 2019. Impact of hydrate saturation on water permeability in hydrate-bearing sediments. Journal of Petroleum Science and Engineering, 174, 696–703. doi: 10.1016/j.petrol.2018.11.084.

McMinn A, Müller MN, Martin A, Ryan KG. 2014. The response of Antarctic Sea ice algae to changes in pH and CO_2. PLoS One, 9(1), e86984. doi: 10.1371/journal.pone.0086984.

Ning YX, Xia ZM, Li XS, Zhao Q, Wan K, Huo D, Zhang N. 2025. Hydrate-based CO_2 sequestration with different water saturation and injection pressure. Energy & Fuels, 39(32), 15277–15287. doi: 10.1021/acs.energyfuels.5c01979.

Nole M, Bartrand J, Naim F, Hammond G. 2025. Modeling commercial-scale CO_2 storage in the gas hydrate stability zone with PFLOTRAN v6. 0. Geoscientific Model Development, 18(5), 1413–1425. doi: 10.5194/gmd-18-1413-2025.

Qanbari F, Pooladi-Darvish M, Tabatabaie SH, Gerami S. 2011. Storage of CO_2 as hydrate beneath the ocean floor. Energy Procedia, 4, 3997–4004. doi: 10.1016/j.egypro.2011.02.340.

Qanbari F, Pooladi-Darvish M, Tabatabaie SH, Gerami S. 2012. CO_2 disposal as hydrate in ocean sediments. Journal of Natural Gas Science and Engineering, 8, 139–149. doi: 10.1016/j.jngse.2011.10.006.

Ryu BJ, Collett TS, Riedel M, Kim GY, Chun JH, Bahk JJ, Lee JY, Kim JH, Yoo DG. 2013. Scientific results of the second gas hydrate drilling expedition in the Ulleung Basin (UBGH2). Marine and Petroleum Geology, 47, 1–20. doi: 10.1016/j.marpetgeo.2013.07.007.

Samset BH, Lund MT, Fuglestvedt JS, Wilcox LJ. 2024. 2023 temperatures reflect steady global warming and internal sea surface temperature variability. Communications Earth & Environment, 5, 460. doi: 10.1038/s43247-024-01637-8.

Sani M, Sani HM, Barau L. 2025. Assessment of climate change effects on human health in Sokoto State, Nigeria. Sokoto Journal of Geographical Studies, 2(1), 55. doi: 10.65760/sjgs.v2.i1.5.

Sawano Y, Wako T, Sato T, Tada K. 2022. Numerical simulation of the effect of gas hydrate formation on liquid-CO_2 leakage suppression in sub-seabed sand sediment. International Journal of Greenhouse Gas Control, 119, 103728. doi: 10.1016/j.ijggc.2022.103728.

Saxena P, Sonwani S, Juhola S, Louis F. 2024. Editorial: Towards 2030: A sustainable cities perspective on achieving sustainable development goal 13–climate action. Frontiers in Sustainable Cities, 6, 1466952. doi: 10.3389/frsc.2024.1466952.

Scafetta N. 2024. Impacts and risks of "realistic" global warming projections for the 21st century. Geoscience Frontiers, 15(2), 101774. doi: 10.1016/j.gsf.2023.101774.

Shi JQ, Durucan S. 2005. CO_2 storage in deep unminable coal seams. Oil & Gas Science and Technology, 60(3), 547–558. doi: 10.2516/ogst:2005037.

Stork AL, Nixon CG, Hawkes CD, Birnie C, White DJ, Schmitt DR, Roberts B. 2018. Is CO_2 injection at Aquistore aseismic? A combined seismological and geomechanical study of early injection operations. International Journal of Greenhouse Gas Control, 75, 107–124. doi: 10.1016/j.ijggc.2018.05.016.

Su M, Wang H, Sha Z, Liang J, Wu N, Qiao S. 2016. Gas hydrates distribution in the Shenhu area, northern South China sea: Comparisons between the eight drilling sites with gas-hydrate petroleum system. Geologica Acta, 14(2), 79–100. doi: 10.1344/GeologicaActa2016.14.2.1.

Sun HR, Chen J, Ji X, Karunakaran G, Chen BB, Ranjith PG, Song YC, Yang MJ. 2024. Optimizing CO_2 hydrate storage: Dynamics and stability of hydrate caps in submarine sediments. Applied Energy, 376, 124309. doi: 10.1016/j.apenergy.2024.124309.

Teng YH, Zhang DX. 2018. Long-term viability of carbon sequestration in deep-sea sediments. Science Advances, 4(7), eaao6588. doi: 10.1126/sciadv.aao6588.

Tohidi B, Yang JH, Salehabadi M, Anderson R, Chapoy A. 2010. CO_2 hydrates could provide secondary safety factor in subsurface sequestration of CO_2. Environmental Science & Technology, 44(4), 1509–1514 doi: 10.1021/es902450j.

Uddin M, Coombe D, Law D, Gunter B. 2008. Numerical studies of gas hydrate formation and decomposition in a geological reservoir. Journal of Energy Resources Technology, 130(3), 032501. doi: 10.1115/1.2956978.

Wang PF, Li Y, Sun NR, Han SB, Wang XM, Su QQ, Li YJ, He J, Yu XH, Du SY, Francisco JS, Zhu JL, Zhao YS. 2024. Hydrate technologies for CO_2 capture and sequestration: Status and perspectives. Chemical Reviews, 124(18), 10363–10385. doi: 10.1021/acs.chemrev.2c00777.

Wei B, Wang BW, Li X, Aishan M, Ju YW. 2023. CO_2 storage in depleted oil and gas reservoirs: A review. Advances in Geo-Energy Research, 9(2), 76–93. doi: 10.46690/ager.2023.08.02.

Wei RP, Shi KJ, Guo XW, Wang T, Lv X, Li QP, Zhang Y, Zhao JF, Yang L. 2021. Evolving thermal conductivity upon formation and decomposition of hydrate in natural marine sediments. Fuel, 302, 121141. doi: 10.1016/j.fuel.2021.121141.

Wu M, Qin Y, Zhang YY, Zhu SF, Zhang GC, Lan FJ, Song XJ, Feng LL, Qin YH. 2023. Influence factors and feasibility evaluation on geological sequestration of CO_2 in coal seams: A review. ACS Omega, 8(19), 16561–16569. doi: 10.1021/acsomega.3c01148.

Xia YQ, Gao P, Jiang ZB, Fan Q, Wei RP, Li QP, Zhang LX, Yu T, Zhao JF, Yang L, Song YC. 2024. Numerical simulation of CO_2 storage in subseabed sediments in the Shenhu area, South China Sea: The effect of reservoir permeability anisotropy. Energy & Fuels, 38(11), 9933–9946. doi: 10.1021/acs.energyfuels.4c00824.

Xia YQ, Yu T, Yang L, Chen BB, Jiang LL, Yang MJ, Song YC. 2025. Multi-state CO_2 distribution patterns for subsea carbon sequestration assisted by large-scale CO_2 hydrate caps. Energy, 320, 135231. doi: 10.1016/j.energy.2025.135231.

Yang F, Bai BJ, Tang DZ, Shari DN, David W. 2010. Characteristics of CO_2 sequestration in saline aquifers. Petroleum Science, 7(1), 83–92. doi: 10.1007/s12182-010-0010-3.

Zhang K, Lau HC. 2022. Sequestering CO_2 as CO_2 hydrate in an offshore saline aquifer by reservoir pressure management. Energy, 239, 122231. doi: 10.1016/j.energy.2021.122231.

Zhang XM, Wang JX, Yang HJ, Li JP, Li YH, Wu QB. 2022. Formation and storage characteristics of CO_2 hydrate in porous media: Effect of liquefaction amount on the formation rate, accumulation amount. Applied Thermal Engineering, 214, 118747. doi: 10.1016/j.applthermaleng.2022.118747.

Zhao GJ, Yang MJ, Pang WX, Gong GJ, Zheng JN, Zhang P, Chen BB. 2022. Effects of hydrate cap on leakage prevention and capacity improvement of sub-seabed CO_2 sequestration. Chemical Engineering Journal, 450, 138493. doi: 10.1016/j.cej.2022.138493.

Zhao GJ, Zheng JN, Gong GJ, Chen BB, Yang MJ, Song YC. 2023. Formation characteristics and leakage termination effects of CO_2 hydrate cap in case of geological sequestration leakage. Applied Energy, 351, 121896. doi: 10.1016/j.apenergy.2023.121896.

Zhao Y, He Q. 2025. Nanostructured materials for carbon neutrality. Nanomaterials, 15(3), 192. doi: 10.3390/nano15030192.

Zhao YF, Itakura KI. 2023. A state-of-the-art review on technology for carbon utilization and storage. Energies, 16(10), 3992. doi: 10.3390/en16103992.

Zheng JJ, Chong ZR, Qureshi MF, Linga P. 2020. Carbon dioxide sequestration via gas hydrates: A potential pathway toward decarbonization. Energy & Fuels, 34(9), 10529–10546. doi: 10.1021/acs.energyfuels.0c02309.

Zhou XB, Fan SS, Xu CL, Wen HY, Chuvilin E, Liang DQ. 2025. Effect of particle size, water saturation, inorganic salt and methane on the phase equilibrium of CO_2 hydrates in sediments. Fluid Phase Equilibria, 588, 114234. doi: 10.1016/j.fluid.2024.114234.